View metadata, citation and similar papers at core.ac.uk

brought to you by CORE

provided by NASA Technical Reports Server

Multiple Velocity Profile Measurements in Hypersonic Flows Using Sequentially-Imaged Fluorescence Tagging

Brett F. Bathel[1]

National Institute of Aerospace and University of Virginia, Hampton, Virginia, 23681

Paul M. Danehy[2], Jennifer A. Inman[3], Stephen B. Jones[4]

NASA Langley Research Center, Hampton, Virginia, 23681-21991

Christopher B. Ivey[5]

Stanford University, Stanford, CA, 94305-3030

and

Christopher P. Goyne[6]

University of Virginia, Charlottesville, Virginia, 22904

Nitric-oxide planar laser-induced fluorescence (NO PLIF) was used to perform velocity measurements in hypersonic flows by generating multiple tagged lines which fluoresce as they convect downstream. For each laser pulse, a single interline, progressive scan intensified CCD (charge-coupled device) camera was used to obtain two sequential images of the NO molecules that had been tagged by the laser. The CCD configuration allowed for sub-microsecond acquisition of both images, resulting in sub-microsecond temporal resolution as well as sub-mm spatial resolution (0.5-mm horizontal, 0.7-mm vertical).

[1] Graduate Student, Mechanical and Aerospace Engineering, NASA Langley Research Center MS 493, AIAA Student Member.
[2] Research Scientist, Advanced Sensing and Optical Measurement Branch, MS 493, AIAA Associate Fellow.
[3] Research Scientist, Advanced Sensing and Optical Measurement Branch, MS 493, AIAA Member.
[4] Technician, Advanced Sensing and Optical Measurement Branch, MS 493.
[5] Graduate Student, Mechanical Engineering, Building 530, 440 Escondido Mall, AIAA Student Member.
[6] Research Assistant Professor, Mechanical and Aerospace Engineering, Aerospace Research Laboratory, PO Box 400248, AIAA Associate Fellow.

Determination of axial velocity was made by application of a cross-correlation analysis of the horizontal shift of individual tagged lines. A numerical study of measured velocity error due to a uniform and linearly-varying collisional rate distribution was performed. Quantification of systematic errors, the contribution of gating/exposure duration errors, and the influence of collision rate on temporal uncertainty were made. Quantification of the spatial uncertainty depended upon the signal-to-noise ratio of the acquired profiles. This velocity measurement technique has been demonstrated for two hypersonic flow experiments: (1) a reaction control system (RCS) jet on an Orion Crew Exploration Vehicle (CEV) wind tunnel model and (2) a 10-degree half-angle wedge containing a 2-mm tall, 4-mm wide cylindrical boundary layer trip. The experiments were performed at the NASA Langley Research Center's 31-Inch Mach 10 Air Tunnel.

Nomenclature

A_{21} = spontaneous emission coefficient, ns^{-1}

C = fluorescence decay correction factor

dt = time step, ns

m = timing index

L = correlation window, pixels

M = total simulation matrix time steps

P = pressure, Pa

Q_{21} = quenching rate, ns^{-1}

R = resolution, m/pixel

S = signal intensity

$S_{1,max}$ = initial maximum signal intensity

$S_{2,max}$ = delayed maximum signal intensity

T = temperature, K

t = time, ns

t_{D1} = first gate delay, ns

t_{D2} = second gate delay, ns

t_{G1} = first gate, ns

t_{eG1} = effective first gate, ns

t_{G2} = second gate, ns

t_P = laser pulse duration, ns

$t_{N-1,\%}$ = student t-statistic

$u_{V,i}$ = *i*-component of velocity uncertainty, m/s

V = velocity, m/s

δt = time step, ns

δx = spatial step, pixels

Δt = timing separation, ns

Δt_{ND} = non-decay timing separation, ns

Δx = spatial separation, pixels

Δx_{ND} = non-decay spatial separation, pixels

τ_{LIF} = fluorescence lifetime, ns

I. Introduction

THE ability to perform quantitative velocity measurements in a hypersonic flow can be complicated by the extreme dynamic and thermodynamic conditions present in hypersonic test facilities and the limited optical access to the test section. Nevertheless, these measurements are needed to validate computational modeling efforts aimed at improved understanding of the physical characteristics of such flows. Recent experimental hypersonic wind tunnel measurement work at NASA Langley Research Center has been focused on providing quantitative velocity data. The NASA Langley Research Center 31-inch Mach 10 blowdown air tunnel is frequently used for both fundamental and project-related testing (i.e. Space Shuttle Orbiter [1], Hyper-X [2], etc.) for which quantitative measurements are beneficial. To date, off-body measurements performed in this facility have been limited to Schlieren imaging [3], pressure rake measurements [4], and more recently nitric oxide planar laser-induced fluorescence (NO PLIF) flow visualization [3].The velocity measurements described in this paper were all performed in this facility using a single laser, single camera, 1-dimensional molecular tagging velocimetry (MTV),

which is a variation of the PLIF technique. The MTV PLIF technique has been shown to be an effective off-wall velocity measurement tool capable of providing spatially-resolved flowfield information [5].The optical access and availability of externally accessible pressure taps for use as a gaseous seeding system make the PLIF technique, and consequently the PLIF-based MTV method, well suited for use in Langley's 31-Inch Mach 10 Air Tunnel.

The single-laser MTV technique, as applied to gaseous flows, was first demonstrated by Hiller et al. [6] to measure velocities below 10 m/s. The experiment utilized laser-induced phosphorescence to tag a single, vertical line of biacetyl molecules and measured the axial displacement of the line over a known time separation (up to 6 ms) to calculate velocity. A single-line, single-laser, flat plate velocity measurement in a hypersonic flow was conducted by Danehy et al. [7] and imaged the displacement of a line of NO fluorescence over a short time separation (250-750 ns). A similar measurement, performed at multiple downstream locations of a supersonic nozzle flow, was performed by Lempert et al. [8] using an acetone tracer to provide an axial velocity map. Inman et al. [9] performed supersonic nozzle velocity measurements simultaneously at several (~22) downstream locations using NO as a tracer. By employing a grid pattern tagged using a biacetyl tracer, Stier and Koochesfahani [10] performed one of the first 2-dimensional MTV experiments.

Several other experiments have used a high-intensity laser pulse to generate a single-line of a particular species gas which can then be tagged by a second laser tuned to an excitation wavelength of these molecules. One such method involves the photodissociation of NO_2 into NO by a high-intensity pulse and was first demonstrated by Orlemann et al. [11] and subsequently employed in gas velocity measurements [12,13]. Recently, Hsu et al. [14] made 2-dimensional supersonic MTV measurements using this technique. Other multi-laser fluorescence methods include air photolysis and recombination tracking (APART) [15,16,17], hydroxyl tagging velocimetry (HTV) [18,19,20], ozone tagging velocimetry (OTV) [21], and Raman excitation and laser-induced electronic fluorescence (RELIEF) [22]. Provided that optical access and sufficient laser energy is available, both one and two-laser techniques can be extended to provide two components of velocity either at a point or in a plane. This is accomplished by creating either a single crossing or grid pattern of intersecting laser lines which can then be analyzed with 2-dimensional cross-correlation algorithm [23].

In addition to obtaining spatial displacement measurements using fluorescence-based MTV, the ratio of collected signal intensities between frames can be used to infer a thermodynamic state variable. Thomson and Maynes [24] performed a single-line laser-induced phosphorescence MTV experiment combined with thermometry. In the

experiment, temperature was determined from a calibration in which the signal intensity along the tagged line was observed over a range of known temperatures. Hu and Koochesfahani [25] and Hu et al. [26] performed a 2-dimensional laser-induced phosphorescence measurement of velocity and temperature about a heated cylinder. In these experiments, the ratio of signal intensities between successive frames was used to exploit the temperature-dependence of the phosphorescence lifetime, and thus infer the temperature field. The use of laser-induced phosphorescence in these experiments was selected due to the relatively long lifetime and temperature sensitivity of the technique. This paper uses a similar signal ratio method to determine instead the error incurred in a 1-dimensional MTV measurement due to collisional quenching.

By slightly modifying the existing NO PLIF flow visualization optical setup installed in the wind tunnel facility, we have been able to perform two separate 1-dimensional MTV experiments providing spatially resolved, quantitative velocity information. The first experiment provided velocity data for a yaw reaction control system (RCS) jet on an Orion Crew Exploration Vehicle (CEV), described in Ref. [27]. In this experiment, a spatial comb filter placed in the path of the laser sheet created a series of shadows to provide velocity profiles. The second experiment provided boundary layer velocity data for a 10-degree half-angle wedge model, described in Refs. [28,29]. For this experiment, the comb filter was replaced with a cylindrical lens array consisting of 25 1-m focal length cylindrical lenses diffusion-welded together. For both experiments, the nominal freestream Mach number was approximately 9.68 with a unit Reynolds number of approximately 1.7×10^6/meter (0.5×10^6/foot).

The purpose of this paper is to report both the demonstration of the MTV technique as applied to two differing hypersonic flows in a large-scale wind tunnel facility and to describe the analysis technique used to determine the velocity profiles and the associated measurement uncertainties. Prior work using the MTV technique has been performed by a number of authors using various techniques to analyze the fluorescence profiles. One particular analysis method, involving the cross-correlation of image pairs to calculate 2-dimensional velocity profiles with sub-pixel accuracy (Ref. [23]), is loosely followed in this paper. However, this correlation approach has been adapted for a one-component velocity measurement. The work reported in this paper makes use of an intensified, double-shutter camera with sequential frame spacing of 500 ns. This removes measurement sensitivity to vibration, which is a potential problem for single-shutter operations. The camera used in this work also eliminates errors that are otherwise associated with a two-camera velocimetry measurement, namely, scaling and shifting the two separately acquired images. We provide, for the first time, an estimation method to compensate for fluorescence

decay and its effect on the spatial shift obtained via the cross-correlation method. To the authors' knowledge, this paper represents the first presentation of single-shot (single laser pulse) velocity measurements with quantified uncertainty using the NO MTV technique.

We will detail the MTV measurement technique by first describing our experimental setup, including the facility, wind tunnel models, laser system, and camera setup. We then describe how scalar velocity values are obtained, how the spectroscopic behavior of the gas changes the measurement and how such behavior is corrected through geometric considerations, along with a full description of the associated uncertainty calculations. Finally, we demonstrate the technique as applied to the CEV and wedge models by providing the spatially and temporally resolved velocity and uncertainty values and present a discussion of these results.

II. Experimental Setup

The complete experimental setup consisted of the optical setup, camera system, two wind tunnel models, the PLIF diagnostic system, and the wind tunnel facility. Discussion of the two wind tunnel models, the PLIF diagnostic system and the wind tunnel facility will be summarized briefly. The camera system and its timing methodology will be discussed in detail in Section II.D.

A. Wind Tunnel Facility

The 31-Inch Mach 10 Air Tunnel is an electrically-heated blowdown facility located at NASA Langley Research Center in Hampton, Virginia, USA. The full details of this facility can be found in the paper by Micol [30], a brief summary of which is provided here. The facility has a nominal Mach number of 10 and a 31-inch square test section and operates on electrically heated, compressed air. Large windows, transparent in the ultraviolet, form three walls (including top, side and bottom) of the test section with the fourth wall formed by the model injection system. The top window allows for the laser sheet to pass through the tunnel section, while the side window allows for imaging of the flow region of interest. The model is side-mounted to the fourth wall. Run durations for the current tests were about one minute. A single facility stagnation pressure, P_0, of 2.41 MPa (350 psia) was investigated for both configurations. The nominal stagnation temperature, T_0, was 1,000 K (1,800 Rankine) for the experiments described herein. Based upon the stagnation conditions, the freestream Mach number was 9.68, the freestream velocity was 1404 m/s, the freestream pressure was 68.3 Pa (9.90×10^{-3} psi), and the freestream temperature was 52.3 K (94.2 Rankine) [30].

B. Wind Tunnel Models

The first experiment was conducted using an Orion Crew Exploration Vehicle (CEV) model [27]. The axis of symmetry of the model was oriented at an 18° angle of attack with respect to the freestream velocity. In this test, only a single yaw RCS jet was analyzed. The RCS jet fluid consisted of a mixture of approximately 5% NO and 95% N_2 and was supplied to the pre-nozzle chamber at a pressure of 0.91 MPa (132 psi). The yaw RCS jet nozzle throat diameter was 0.7-mm (0.0275-inch) with an exit-to-throat area ratio of 22.5.

The second experiment was conducted using a 10° half-angle wedge model with a sharp leading edge, similar to that described in Ref. [28]. A 2-mm tall, 4-mm wide cylindrical boundary layer trip was positioned along the centerline 75.4-mm downstream of the leading edge (measured to the center axis-of-symmetry of the trip) to deflect the laminar boundary layer gas. The seeded gas was 100% NO, supplied at 150 SCCM (standard cubic centimeters per minute), and was seeded into the laminar boundary layer from an 11-mm-long, 0.81-mm-wide spanwise slot located 29.4-mm downstream of the leading edge. The flowrate supplied through this slot was assumed to minimally perturb the boundary layer flow. This assumption is based in part upon surface heat transfer measurements performed by Berry et al. [31] using a similar gas supply configuration. Analysis of these heat transfer measurement results and the degree of boundary layer perturbation associated with different gas-injection flow rates for the present wedge model are discussed by Danehy et al. [29].

C. PLIF System

A pulsed Spectra Physics Pro-230 Nd:YAG laser was used to pump a Sirah Cobra Stretch dye laser at 532 nm to achieve a 622 nm output beam. This output was mixed with 355 nm light from the Nd:YAG in a Sirah Frequency Conversion Unit to produce ~5 mJ per pulse at 226 nm. This beam was directed to the sheet-forming optics affixed above the tunnel test section. The duration of the pulse at this wavelength was approximately 9.5 ns.

To form a laser sheet, the collimated 226 nm beam was passed through a 36-mm focal length cylindrical lens, which expanded the beam in one direction while leaving it collimated in the other. A 1-m spherical lens then collimated the diverging axis of the beam and focused the other axis into a thin sheet approximately 75-mm wide by 0.5-mm thick. To tag multiple lines of NO in the test section for a velocimetry measurement, either a spatial comb filter or lens array was placed below the sheet-forming optics. For the Orion CEV test, a spatial comb filter was used to create the series of vertical shadows. For the wedge model, a 50-mm-long, LaserOptik diffusion-welded lens array of 25, 1-m focal length cylindrical lenses focused the laser sheet into 25 lines, running parallel to the model

surface and propagating in the spanwise direction. The lens array had an anti-reflection coating. The lines formed with each method typically had widths of approximately 1.1 mm at FWHM (full width at half maximum), with a 2.5-mm separation distance between each line.

D. Camera System and Timing

To image the tagged lines in both experiments, a Cooke DiCAM-PRO camera, utilizing an intensified 1280x1024 pixel array interline progressive scan CCD, was used. For the wedge model, only a 1280x256 pixel region was used to image the flow so that an image read-out rate of 10 Hz, corresponding to the laser pulse frequency, could be achieved. Similarly, a 1280x288 pixel region was used for the CEV experiment. A 105-mm focal length, F/4.5 Nikon UV Nikkor lens was used for the CEV experiment and a 100-mm focal length, F/2.0 B. Halle Nachfl. lens was used for the wedge experiment. Spatial resolutions were 17.3 pixels/mm (439.4 pixels/inch) and 17.5 pixels/mm (444.5 pixels/inch) for the CEV and wedge model experiments, respectively. When used in double shutter mode, the camera is capable of acquiring an image pair with a minimum 500 ns delay between the end of the first gate and the beginning of the second. Each gate has a minimum duration of 20 ns, with delay settings and durations controllable in increments of 20 ns.

After the NO gas is excited by a laser pulse, the fluorescence intensity decays exponentially in time. The rate of this decay depends upon the local pressure, temperature, and gas composition influencing the tagged molecules. The camera used in these experiments did not allow for independent gain settings for the first and second exposures. To ensure a measurable signal during the second exposure, it was necessary to use the minimum gate delay setting of 500 ns and keep the second gate open long enough to collect an adequate number of photons. Additionally, to maintain comparable signal intensities in both the first and second CCD exposures, the signal in the first exposure had to be attenuated. This was partly achieved by using the shortest gate possible (20 ns). Additionally, the timing of the first gate was such that it opened prior to the laser pulse and then collected fluorescence only during the first several nanoseconds of the laser pulse. This overlap of the first exposure and laser pulse is achieved by simultaneously triggering the camera and laser with a LabSmith LC880. The camera software then allowed coarse adjustment of the relative timing of the laser and first camera gate, in 20 ns increments. Fine adjustments on the order of 1 ns were then made by adding varying lengths of coaxial cable between the LC880 and the camera trigger input, The resulting overlap of the first camera gate and the laser pulse is referred to as the *effective 1st gate*, having a duration of t_{eG1}. During experimentation, care was taken to avoid saturation of the CCD.

Table 1 gives the timing parameters used in the experiments. Figure 1 shows a generalized timing sequence adopted for these experiments. The vertical axis represents signal intensity, with the solid black line showing the exponential decay behavior of fluorescence with time. The darkly shaded regions represent the signal intensity captured during the first and second exposures. The lightly shaded regions are indicative of the first and second gate durations, respectively, while the region with the dashed black border indicates the laser pulse duration, t_p.

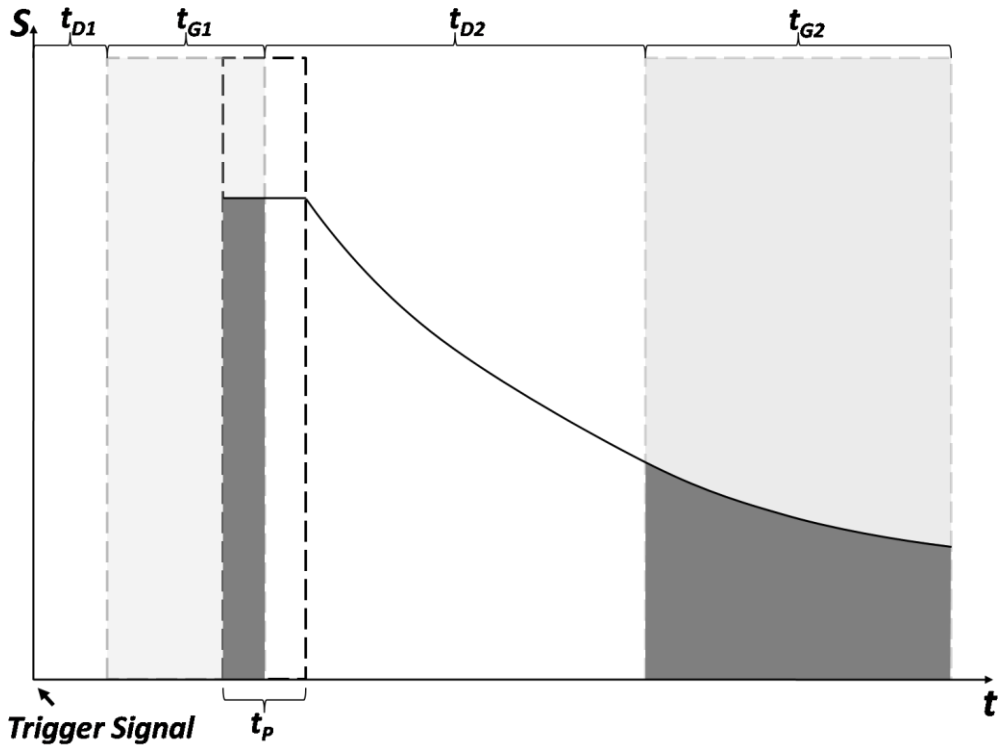

Fig. 1 Camera and laser timing sequence and signal intensity.

Table 1. Laser and camera timing parameters

Laser Pulse Duration, t_P	9.5 ns
1st Gate, t_{G1}	20 ns
Effective 1st Gate, t_{G1}	8.25 ns (CEV) 10.25 ns (Wedge)
2nd Delay, t_{G2}	500 ns
2nd Gate, t_{G2}	300 ns (CEV) 100 ns (Wedge)
Resolution	1280 x 288 pixels @ 17.3 pixels/mm (CEV) 1280 x 256 pixels @ 17.5 pixels/mm (Wedge)

III. Velocity Analysis

Determination of the axial velocity is based upon a time-of-flight calculation in which the measured distance between the center of mass of the profile observed in the undelayed (first) and delayed (second) images, Δx_{ND}, is

divided by the time separating their acquisition, Δt_{ND}, where the subscript *ND* means "no decay" and refers to the respective parameter determined in the absence of any fluorescence decay. The velocity relation is therefore:

$$V = \frac{\Delta x_{ND}}{\Delta t_{ND}} \tag{1}$$

Obtaining values for Δx_{ND} and Δt_{ND} will be described below in sections B and C, respectively.

A. Image Pre-Processing

The spatial resolution for both experiments was measured by acquiring an image of a matrix of square marks separated at equal spatial intervals, known as a *dotcard* and described in Ref. [32]. When these spatial calibration images were acquired, the dotcard was placed in the plane of the laser sheet, later used to interrogate the seeded NO gas.

To correct for optical and perspective distortion of the images in the wedge experiment, the image of the dotcard in the test section was acquired with the camera and a corresponding undistorted image of the same dotcard was created with Adobe Acrobat software. An image registration algorithm, *UnwarpJ* (Ref. [33]), was then used to correct the distortion. This software is a plug-in created for the image processing software, *ImageJ*, a freeware image processing program available from National Institutes of Health [34]. The image registration algorithm was not applied to the RCS velocity experiment images.

To improve the signal-to-noise ratio in the images, MATLAB® was used to apply a 4-pixel radius average disk filter to the undelayed and delayed fluorescence images. The images were then binned by 4 pixels in the vertical direction. These two steps improved the signal-to-noise by smoothing camera noise and consolidating the signal in regions tagged by the laser. This provided approximate streamwise and spanwise spatial resolutions of 0.5-mm and 0.7-mm, respectively.

Prior to processing each image for velocity information, a background offset level was subtracted from the undelayed and delayed images. For the wedge experiment, the background level was obtained from images taken with the laser blocked. For the CEV experiment, the background level was obtained from a region where no laser illumination was present. Due to the shortness of the gate delay used between the undelayed and delayed images (500 ns) and the relatively long decay time of the P46 phosphor in the intensifier, some ghosting remained from the undelayed image in the delayed image. For the 500 ns gate delay, this level was experimentally determined to be

approximately 1/126th of the undelayed image. Therefore, this fraction of the undelayed image was also subtracted from the delayed image in addition to the background offset level.

B. Spatial Analysis

To obtain the relative shift between individual lines in the undelayed and delayed image, a 45-pixel-wide window was selected that encompassed each vertical tagged line in the undelayed image. For each row of pixels in this window, an undelayed fluorescence profile was obtained. This window was positioned encompassed the same pixel region in the delayed image, with the delayed fluorescence profiles again acquired for each row in the window. The center of this window was positioned approximately 5 pixels to the right of the of the line center in the undelayed image. This was done to minimize clipping either side of the initial or delayed profile. A user defined threshold, applied to the maximum pixel intensity for each row in the undelayed image, was used to reject low signal profiles which might otherwise provide poor quality velocity information. In these cases, no velocity information is reported.

For each remaining profile pair, each of length L = 45 pixels, a cross-correlation was performed using MATLAB®'s *xcorr* function. The maximum value resulting from the array (of length $2L + 1 = 91$ pixels) of cross-correlation coefficient values then was found and a 7th-order polynomial fit, centered about this maximum, similar to the method used by Gendrich and Koochesfahani [23], was obtained. For this analysis, 11 points (centered about the maximum) were used to compute the polynomial fit. Setting the first derivative of this polynomial equal to zero and using a root-finding algorithm to determine the maxima of the polynomial fit, the resolved maximum of the coefficient values was obtained. The resulting difference between this resolved maximum and the length of the input profile vector corresponds to the total shift, in pixels, of each profile pair.

To obtain the average spatial displacement, in time, at a particular location along a tagged profile in the flowfield, the mean spatial shift for a set of N image pairs was calculated.

C. Timing Simulation and Analysis

1. *Phenomenological derivation of displacement (neglecting fluorescence decay)*

In the absence of fluorescence decay, a phenomenological geometric argument can be made, based upon the camera and laser timing parameters selected, to describe the elapsed time between the undelayed and delayed images. This approach is a refinement of that of Danehy et al. [7]. Figure 2 shows two space-time-signal diagrams describing an infinitesimal spatial width laser beam exciting fluorescence at a rate of 1 block of molecules per unit

of time. The axes are x for space, t for time, and S for PLIF signal intensity. The vertical plane along the time axis in Figs. 2a and 2b shows the relative timing of the first gate, laser pulse, and second gate, which are represented by the shaded areas with dashed borders.

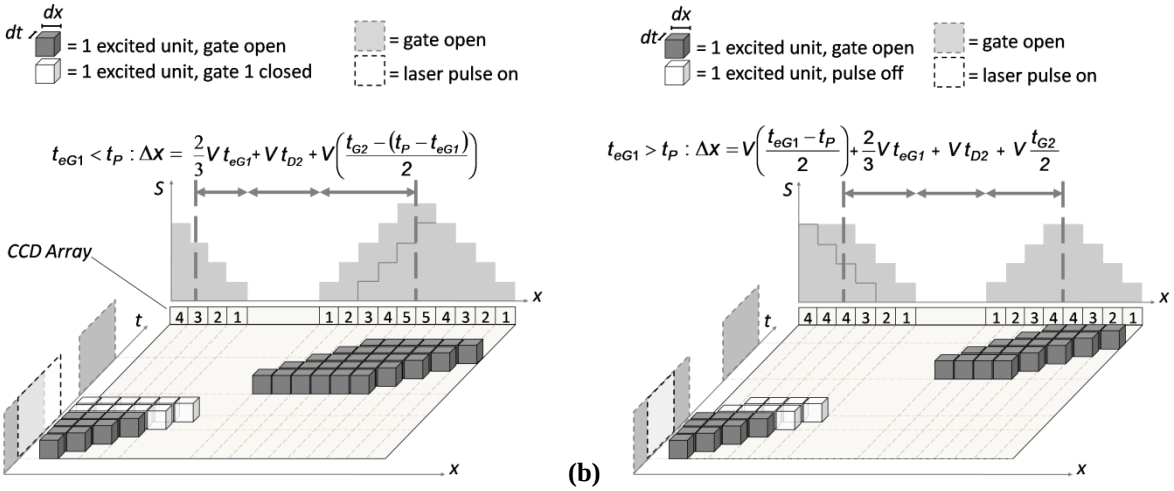

Fig. 2 Space-time-signal diagram of idealized CCD signal and acquisition of fluorescence with effective 1st gate shorter (a) and longer (b) than laser pulse.

The blocks, which represent a 1-dimensional region of NO gas moving left-to-right, are shaded according to the means by which they emit fluorescence photons. The gray blocks in the lower left-hand region of the space-time diagram are excited and emit photons captured by the CCD camera during the overlap period of the first camera gate and the laser pulse. In Fig. 2a, the white blocks are excited and emit fluorescence while the laser pulse continues, but after the first camera gate has been closed (that is, they are not captured by the first camera gate). In Fig. 2b, the white blocks are excited and emit fluorescence after the laser pulse has ceased, but before the first camera gate has been closed. The gray blocks in the upper right-hand region of the space-time diagram represent fluorescence captured during the second camera gate.

During the laser pulse, if a non-zero axial velocity is present, in the absence of fluorescence decay, each block of NO gas is assumed to be excited instantaneously by the pulse and convected one spatial unit, Δx_{ND}, downstream per unit of time, Δt_{ND}, with the ratio corresponding to the axial velocity, $V = \Delta x_{ND}/\Delta t_{ND}$.

At each time step in this process, the emitted fluorescence from each block is captured by a pixel on the camera CCD array. During the first camera gate, the blocks of NO gas are excited by the laser and then convected downstream. If the effective 1st gate is less than or equal to the pulse duration (Fig. 2a) then resulting intensity distribution along a row of pixels on the CCD takes on a right triangle-like profile. If the effective 1st gate is greater than the pulse duration (Fig. 2b) then the right triangle-like profile becomes subject to some level of blurring across

the pixels. In Fig. 2, this charge distribution is represented by the light-gray shaded area on the signal-spatial axis. The numbers, located directly below this area, are segmented into pixels along an array of the CCD and represent the total charge accumulated (in arbitrary units) during the two exposures (the right triangle-like profile corresponding to the 1st exposure and the trapezoidal profile corresponding to the second exposure).

In Fig. 2a, after the 1st camera gate has closed, a total of four blocks of NO gas have been excited by the laser pulse. As the rectangular-shaped laser pulse continues for an additional two time units, and additional two blocks of NO gas are excited, resulting in a train of excited NO gas that is a total of six blocks long. In Fig. 2b, after the laser pulse has ceased, four blocks of NO have been excited. For the remainder of the effective 1st gate, this train of excited NO gas continues to progress downstream with its fluorescence captured by the CCD.

After the end of the laser pulse, the train of NO gas is convected. Then, the second camera gate is opened and the train of NO gas continues to convect downstream while the fluorescence is again captured by the CCD pixels. In this case, the charge distribution across the pixels takes on a trapezoidal shape, as shown in the shaded area of the signal-spatial axis in Figs. 2a and 2b. Note that in Fig. 2a, if the end of the laser pulse had coincided with the end of the first camera gate, the NO gas would have been a 4-block train and the profile shape observed in the second camera gate would instead appear to be narrower and weighted to the right. This alternate profile shape is represented by the shaded area falling under the dark segmented line in Fig. 2a. If the effective 1st gate exceeds the pulse duration, as in Fig. 2b, the profile observed in the first exposure would appear to be weighted to the right due to blurring of the 4-block train. This right-weighted profile shape is shown extending to the left of the dark vertical line in Fig. 2b.

Based upon this timing sequence, which neglects fluorescence decay due to quenching, the apparent distance between the center of mass of the fluorescence profiles acquired during the first and second camera gates is:

$$\Delta x_{ND} = V \cdot \left(\frac{2}{3} t_{eG1} + t_{D2} + \frac{t_{G2}}{2} - \frac{(t_P - t_{eG1})}{2}\right) = V \cdot \Delta t_{ND} \tag{2}$$

In this example, $2t_{eG1}/3$ corresponds to the center of mass of the right triangle profile observed in the first exposure, t_{D2} is the delay between the end of the first and start of the second exposures (typically 500 ns), and $t_{G2}/2$ is the center of mass of the profile observed in the second exposure. The $-(t_P - t_{eG1})/2$ term corresponds to the added weighting of either the second exposure profile if $t_P > t_{eG1}$ or the first exposure profile if $t_P < t_{eG1}$. By dividing both sides of the equation by the velocity, V, an expression for the effective time between the first and second camera gates is obtained.

2. *Simulation and validation of the effect of fluorescence decay*

If relatively uniform thermodynamic conditions exist over the imaged region of a flow moving from left to right, fluorescence decay causes the perceived center of mass of the intensity profile observed in both the first and second image to become slightly left-weighted, with the effect being much more apparent in the second image. This is because the fluorescence intensity of the tagged gas region decays exponentially in time. Therefore, as the gas is convected downstream, the upstream pixels receive more fluorescence than the downstream pixels. Figure 3a shows a simulated CCD exposure in which a spatially narrow top-hat beam is used to excite NO molecules being convected from left to right. This simulated second exposure, beginning 500 ns after the end of the first gate, shows the resulting fluorescence profiles observed with (solid black) and without (dotted gray) the effect of decay. The simulation is exaggerated to emphasize that an error can result if care is not taken to compensate for the effect of fluorescence decay. Figure 3b shows a simulation involving a more realistic 19-pixel wide (FWHM) Gaussian beam profile with (solid black) and without (dotted gray) fluorescence decay.

Prior to simulating the first exposure, a zero-valued matrix consisting of $M = t_{eG1}/\delta t$ rows and L columns was initialized. For each time step, the intensity distribution was added to the m^{th} row of a *profile matrix*, initially a matrix of zeros, and then progressed by $\Delta X = V \cdot (m-1)\delta t$. The process was repeated for the duration of the effective 1st gate from m = 1 to M. At each row, a cumulative summation including all subsequent rows was then performed. This summation represented the contribution of a single blurred profile instantaneously created at the m^{th} time step. Using this summation matrix, a final summation was performed from rows $m = 1$ through $m = t_P/\delta t$ to create the first *exposure array*.

For the second exposure, a profile matrix was again generated consisting of $M = (t_{G2} + t_P)/\delta t$ rows and L columns. For each time step, the intensity distribution was added to the m^{th} row and then progressed spatially by $\Delta X = V \cdot [t_{D2} - (t_P - t_{eG1}) + (m-1)\delta t]$. An array was then calculated by performing a summation over a total of $t_{G2}/\delta t$ rows, and repeating this summation beginning at the first row and proceeding to the $m = t_P/\delta t$ row, adding each summation to the previous array, ultimately resulting in the second exposure array.

For both the first and second profile array, the intensity distribution at each time step was multiplied by the exponential decay factor:

$$exp\left(-\frac{(m-1)\cdot\delta t}{\tau_{LIF}}\right)$$

$$\tau_{LIF} = \frac{1}{A_{21}+Q_{21}} \tag{3}$$

where m is the current time step of the simulation, τ_{LIF} the fluorescence lifetime, Q_{21} is the pressure/temperature-dependent collisional quenching rate, and A_{21} = 192.6 ns^{-1} is the spontaneous emission rate. Values for Q_{21} and A_{21} were obtained from Settersten et al. [35,36]

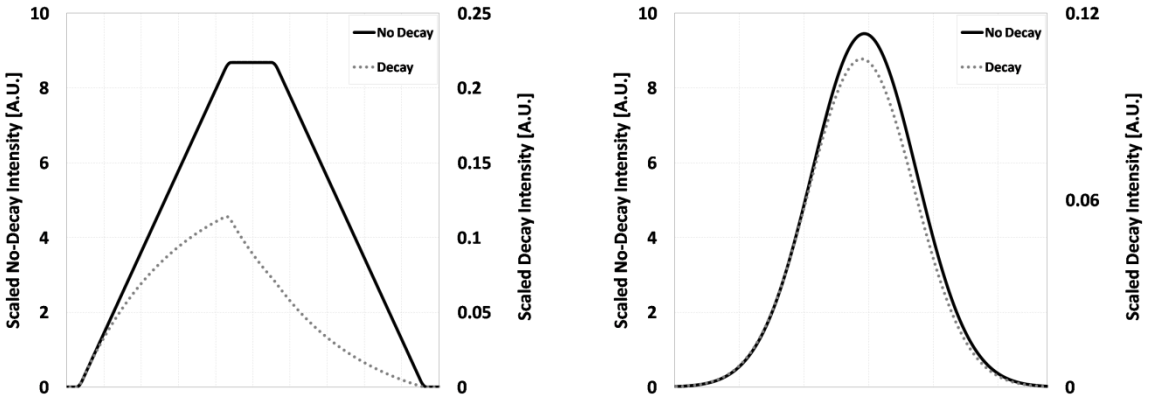

Fig. 3 Simulated CCD exposure using (a) a narrow top-hat spatial laser profile and (b) a Gaussian 19-pixel FWHM spatial laser profile.

For these simulations, $\boldsymbol{t_P}$ and $\boldsymbol{t_{D2}}$ were fixed at 9.5 ns and 500 ns, respectively. A temporal spacing of $\boldsymbol{\delta t}$ = 0.05 ns was used with a grid spacing of $\boldsymbol{\delta x}$ = 0.01 pixels, corresponding to 0.6 μm experimentally. For the range of velocities used in the simulation, care was taken to satisfy the Courant-Friedrichs-Lewy (CFL) condition and a discretization density study was performed to ensure grid independence. The simulated laser excitation source had an intensity distribution approximated by a Gaussian spatial profile with a FWHM of 19 pixels located -2 pixels from the center of the correlation window. To estimate the effective 1st gate duration for the simulation corresponding to the wedge and CEV tests, experimental signal ratios over a range of pressures at 298 K from a near-zero velocity field were obtained. These were then compared with simulated signal ratios over the same pressure range and temperature, but for multiple values for $\boldsymbol{t_{eG1}}$. From this, it was determined that the effective 1st gate duration for the CEV and wedge experiments was 8.25 ns and 10.25 ns, respectively. Figure 4 shows the result of this validation.

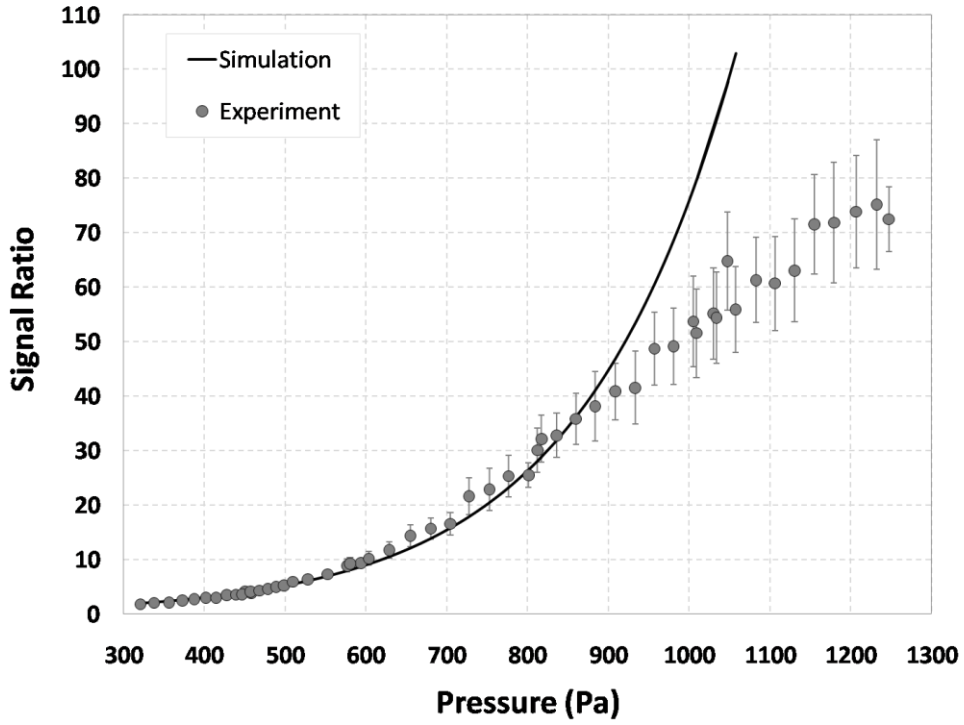

Fig. 4 Comparison of simulated and experimental signal ratio (first gate intensity divided by second gate intensity) as a function of pressure. Temperature is a constant 298 K.

3. *Use of signal ratio to correct for effects of fluorescence decay*

If the fluorescence lifetime is known, the apparent shift in the center of mass of the fluorescence profile can be estimated by simulating the fluorescence acquired by both camera exposures, as described in Section III.C.2. By performing such a simulation, which accounts for blurring due to finite (non-infinitesimal) gate duration, a relation between the ratio of the maximum signal intensities of the undelayed and delayed frames and the fluorescence lifetime can be formulated. However, if the experimental fluorescence lifetime is not known, a simulation using the experimental camera timing parameters can be used to estimate the profile shape and signal intensity ratio for several different lifetimes. Using this approach, an experimentally obtained signal ratio can be used in conjunction with the simulation results to infer the fluorescence lifetime. With the known fluorescence lifetime, the simulation can then provide an estimate for the level of compensation needed to correct for the perceived profile shift. This paper uses the simulation approach to estimate the profile shifts observed experimentally. A range of fluorescence lifetimes corresponding to conditions encountered during typical wind tunnel tests were simulated for three different second-gate durations: 100 ns, 200 ns, and 300 ns.

Figure 4 shows that above pressures of 900 Pa, a significant deviation from the simulated signal ratio trend occurs. This corresponds to $\tau_{LIF} < 74$ ns. For the test conditions reported in this paper, fluorescence lifetimes remained above this lower lifetime limit. The primary trend, however, is that as pressure increases, the signal observed during the second gate decreases, causing the ratio to increase.

Once the first and second simulated exposures with and without fluorescence decay were obtained, the cross-correlation algorithm described in the previous section was then applied to the simulated first and second exposures to determine the relative shift. For an arbitrarily simulated velocity magnitude, V, the time separation in the absence of fluorescence decay is known (Δt_{ND}), and the ratio of relative spatial shift obtained from the simulated exposures with (Δx) and without (Δx_{ND}) fluorescence decay, along with the result of Equation 2, provides the following relationship:

$$V = \frac{\Delta x}{C \cdot \Delta t_{ND}} = \frac{\Delta x_{ND}}{\Delta t_{ND}} \tag{4}$$

where the fluorescence decay correction factor, C, is used in the analysis to correct the time separation between exposures. Thus, the relation in Equation 4 simplifies to:

$$C = \frac{\Delta x}{\Delta x_{ND}} \tag{5}$$

The coefficient, C, was determined from the simulation by analyzing the ratio of maximum signal intensities in the undelayed, $S_{1,max}$, and delayed, $S_{2,max}$, profiles and relating it to the profile shifts, Δx and Δx_{ND}. Based upon analysis of experimental profiles, the ratio of intensity values, $S_{1,max}/S_{2,max}$, can be used, in conjunction with the simulation results, to measure of the NO fluorescence lifetime, τ_{LIF}, and then infer the magnitude of apparent shift due to fluorescence decay. Using this methodology, the following relation between signal intensity ratio and correction factor was obtained using TableCurve 2D®:

$$C = a + b\left(\frac{S_{1,max}}{S_{2,max}}\right)^{1/2} + c\ln\left(\frac{S_{1,max}}{S_{2,max}}\right) \tag{6}$$

where the coefficient values for a, b, and c, for a particular t_{eG1} and t_P, vary with the second gate duration, t_{G2}. Table 2 provides the coefficient values used to compute the correction factor the CEV and wedge experiments. Figure 5 shows the behavior of this correction factor as a function of fluorescence lifetime. Curves for an effective

1st gate of 8.25 ns and second gate durations of 100 ns, 200 ns, and 300 ns are shown. Figure 5 shows that the effect of fluorescence decay, and thus of the correction factor, is most pronounced for short fluorescence lifetimes and long exposure times.

Table 2. Correction factor coefficients.

Coefficent	CEV (t_{eG1}=8.25, t_{G2}= 300 ns)	Wedge (t_{eG1}=10.25, t_{G2} = 100 ns)
a	9.218×10^{-1}	9.920×10^{-1}
b	2.309×10^{-3}	4.247×10^{-5}
c	-1.636×10^{-2}	-2.731×10^{-3}

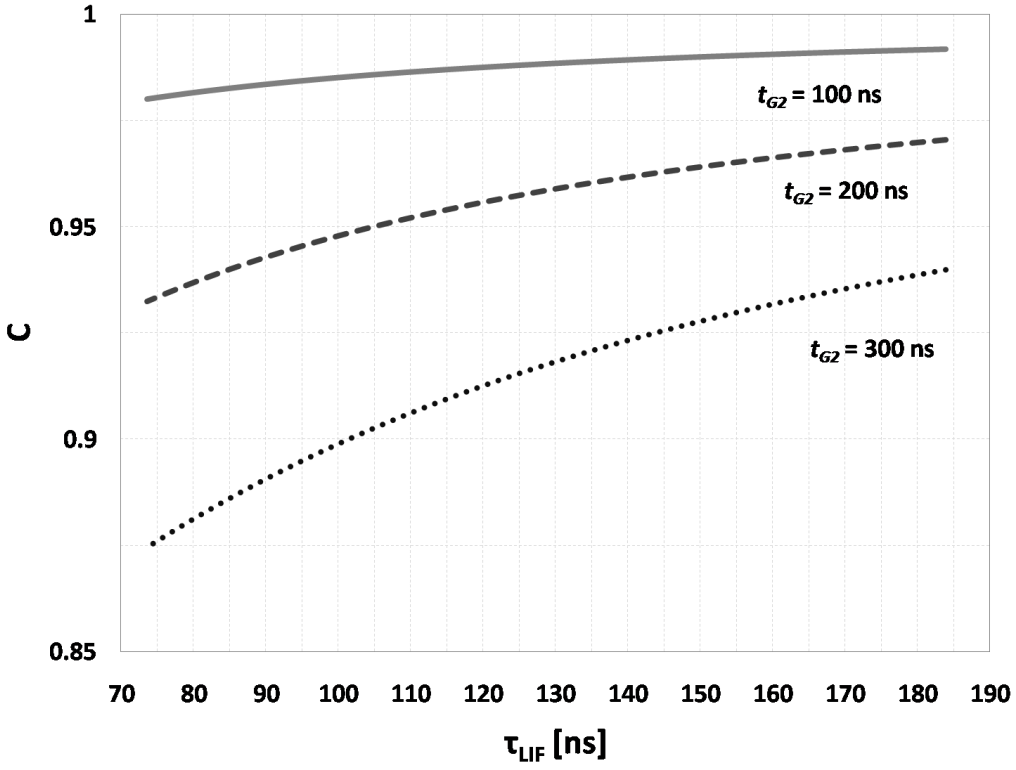

Fig. 5 Variation of timing correction factor used for CEV experiment as a function of fluorescence lifetime.

IV. Uncertainty Analysis

The velocity uncertainty was based upon the contributions of magnification, accuracy errors, errors associated with spanwise velocity components, and the contributions of spatial and temporal uncertainties. The general form of the velocity uncertainty is:

$$u_V = u_{V,\text{Magnification}} + u_{V,\text{Accuracy}} + u_{V,\text{Spanwise}} + \sqrt{u_{V,\Delta x}^2 + u_{V,\Delta t}^2} \tag{7}$$

A. Spatial Uncertainty

The uncertainty in velocity due to spatial uncertainties, $u_{V,\Delta x}$, was obtained by first determining the spatial shift, Δx_i, along each fluorescence profile for each single-shot image. The single-shot and average spatial uncertainties at 95% confidence for a particular location were determined, respectively, by analyzing the sensitivity of the measured velocity to variations in spatial shift:

$$u_{V,\Delta x} = \frac{\partial V}{\partial(\Delta x)} \cdot u_{\Delta x} = \frac{1}{C \cdot \Delta t_{ND}} \cdot t_{N-1,95\%} \sqrt{\frac{\sum_{i=1}^{N} (\Delta x_i - \overline{\Delta x})^2}{N-1}} = \frac{t_{N-1,95\%} \cdot \sigma_{\Delta x}}{C \cdot \Delta t_{ND}}$$
$$u_{V,\overline{\Delta x}} = \frac{u_{V,\Delta x}}{\sqrt{N}} \tag{8}$$

where the product of the standard deviation, $\sigma_{\Delta x}$, and the student t-distribution value at 95% confidence, $t_{N-1,95\%}$, represents the uncertainty in each spatial and temporal variable. In this equation N represents the number of resolved single-shot velocity measurements at a particular point in the flow field, which can vary from point to point, and is less than or equal to the number of single-shot images being analyzed.

B. Timing Uncertainty

The uncertainty in velocity due to uncertainties in the time separation, $\boldsymbol{\Delta t}$, includes systematic uncertainties resulting from camera and laser timing jitters and duration uncertainties as well as uncertainty due to variations in signal intensities, which are used to infer the lifetime and calculate the correction factor, $\boldsymbol{C}$. The definition of the uncertainty in velocity due the timing separation is:

$$u_{V,\Delta t} = \frac{\partial V}{\partial(\Delta t)} \cdot u_{\Delta t} \tag{9}$$

and the net temporal uncertainty, $u_{\Delta t}$, can be defined as:

$$u_{\Delta t} = \sqrt{u_{\Delta t,C}^2 + u_{\Delta t_{D1}}^2 + \left(\frac{2 \cdot C \cdot u_{\Delta t_{eG1}}}{3}\right)^2 + \left(C \cdot u_{\Delta t_{D2}}\right)^2 + \left(\frac{C \cdot u_{\Delta t_{G2}}}{2}\right)^2 + \left(\frac{C \cdot u_{\Delta t_P}}{2}\right)^2 + \left(\frac{C \cdot u_{\Delta t_{eG1}}}{2}\right)^2} \tag{10}$$

where the uncertainty due to correction factor, $u_{\Delta t_C}$, is defined below. The remaining timing uncertainties are defined in Table 3. The root-sum-squared of the individual temporal uncertainties is applied to calculate the net temporal uncertainty because of the random nature of the individual uncertainties encountered during acquisition of the data.

Table 3. Laser and camera timing uncertainties

Laser Pulse Jitter, $u_{\Delta t_P}$	±0.1 ns
1st Delay Jitter, $u_{\Delta t_{D1}}$	±2.0 ns
Effective 1st Gate Duration, $u_{\Delta t_{eG1}}$	±1.0 ns
2nd Delay Jitter, $u_{\Delta t_{D2}}$	±0.5 ns
2nd Gate Duration, $u_{\Delta t_{G2}}$	±1.0 ns

On a shot-to-shot basis, variation in the signal intensity between the undelayed image and delayed image at a point in the tagged profiles results in a variation in the correction factor. This results in apparent variations to the elapsed time between images. To minimize the magnitude of this variation, the second gate duration can be decreased, as was done in the wedge model experiment. In Fig. 5, as the second gate duration is decreased, the variation in correction factor as a function of fluorescence lifetime decreases. The single-shot uncertainty associated with the correction factor, $u_{\Delta t,C}$, at a point is calculated in the following equations.

$$u_{\Delta t,C} = \frac{\partial(\Delta t)}{\partial C} \cdot u_C = (\Delta t_{ND}) \cdot u_C \tag{11}$$

where u_C is the uncertainty in the correction factor. Further expanding this term gives:

$$u_C = \frac{\partial C}{\partial(S_{1,max}/S_{2,max})} \cdot u_{(S_{1,max}/S_{2,max})}$$

$$u_{(S_{1,max}/S_{2,max})} = \sqrt{\left(\frac{\partial(S_{1,max}/S_{2,max})}{\partial S_{1,max}} \cdot u_{S_{1,max}}\right)^2 + \left(\frac{\partial(S_{1,max}/S_{2,max})}{\partial S_{2,max}} \cdot u_{S_{2,max}}\right)^2} \tag{12}$$

$$u_{S_{l,max}} = t_{N-1,95\%} \sqrt{\frac{\sum_{i=1}^{N}\left(S_{l,max_i} - \overline{S_{l,max}}\right)^2}{N-1}} \quad l = 1,2$$

where u_C is based on the functional form of the correction factor, C, in Equation 6.

The average correction factor uncertainty at a point for *N* resolved velocity measurements was determined in a similar manner:

$$u_C = \frac{\partial C}{\partial(S_{1,max}/S_{2,max})} \cdot u_{\overline{S_{l,max}}}$$

$$u_{\overline{S_{l,max}}} = \frac{u_{S_{l,max}}}{\sqrt{N}} \quad l = 1,2 \tag{13}$$

The variation in the camera and laser timing also contributed to the temporal uncertainty. Table 3 gives the magnitude of camera and laser timing and jitters and duration uncertainties used in the uncertainty analysis, with the largest contribution being from the jitter in the delay of the first gate. This jitter affected the overlap of the first gate and the laser pulse, as shown in Fig. 1, by varying the start of the first gate. Incorporation of these uncertainties is given in Equation 10. The timing and spatial uncertainties are grouped in the root-sum-squared term in Equation 7, and represent the uncertainty in velocity precision.

C. Velocity Accuracy

To determine the uncertainty due to magnification, several measurements were taken at nine different locations on the dotcard images. The average magnification and the standard deviation of the magnification, $\sigma_{\text{Magnification}}$, for the CEV and wedge model tests is given in Table 4. The general form of the magnification uncertainty for both experiments, using 9 measurements (8 degrees-of-freedom) at 95% confidence was:

$$u_{\text{V,Magnification}} = \frac{\partial V}{\partial R} u_{\text{Magnification}} = \frac{(\Delta x)_{PIXEL}}{C \cdot \Delta t_{ND}} \cdot \sigma_{\text{Magnification}} \cdot t_{8,95\%} \tag{14}$$

where $(\Delta x)_{PIXEL}$ is the pixel shift between profiles in the undelayed and delayed images of the processed images. This uncertainty scales linearly with the measured pixel shift between the undelayed and delayed images. Table 4 provides an upper-bound estimation of the uncertainty in velocity due to magnification error considering a maximum velocity of 790 m/s for the CEV experiment and 1260 m/s for the wedge experiment.

To estimate the accuracy of the cross-correlation technique as applied to the CEV and wedge experiments, velocity images were obtained while the wind tunnel was not operating, resulting in (nearly) static gas. While these images were collected, the tunnel pressure slowly increased from approximately 320 Pa to 1250 Pa. This was due to leaks present in the tunnel section when the pressure was reduced to near vacuum, and created the potential for small velocities within the test section. The images were then analyzed with the cross-correlation software to determine the velocity and uncertainty, as well as the signal ratio data provided in Fig. 4. Figure 6 shows the results of this zero-velocity analysis over the range of pressures tested. Based upon the mean velocity analysis, the accuracy was estimated to be ±10 m/s, shown by the accuracy bounds in Fig. 6. Table 4 also lists this accuracy value.

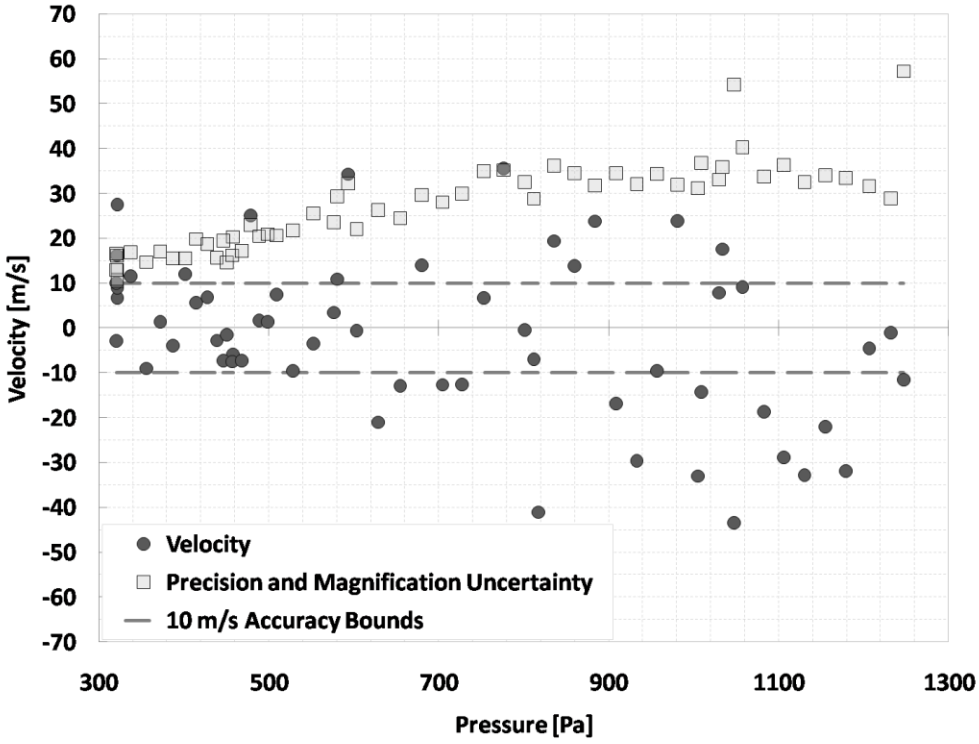

Fig. 6 Velocity accuracy data obtained from low pressure, no-flow wind tunnel test.

Table 4. Magnification and accuracy values.

CEV	Mean Magnification	5.75×10^{-2} mm/pixel
	Standard Deviation, $\sigma_{\text{Magnification}}$	$\pm 5.06 \times 10^{-5}$ mm/pixel
	Maximum Uncertainty, $u_{V,\text{Magnification}}$	±1.12 m/s
Wedge	Mean Magnification	5.70×10^{-2} mm/pixel
	Standard Deviation, $\sigma_{\text{Magnification}}$	$\pm 3.67 \times 10^{-5}$ mm/pixel
	Maximum Uncertainty, $u_{V,\text{Magnification}}$	±1.49 m/s
	Accuracy, $u_{V,Acc}$	±10 m/s

D. Spanwise Velocity Uncertainty

In addition to estimating the axial velocity uncertainty, uncertainty due to unmeasured spanwise velocity components (parallel to the laser beam) must also be included. This uncertainty is a result of gas being convected in the spanwise direction between the undelayed and delayed frames. If a portion of the tagged profile at a particular location has moved in the spanwise direction after the first gate has closed, it will be incorrectly correlated with the portion of the undelayed image at the same spanwise location in the delayed image. This uncertainty will be most notable in regions of the flow with steep axial velocity gradients.

To obtain a refined estimate of this uncertainty, it was assumed that the only significant velocity components existed in the axial and spanwise directions. For this analysis, the difference between the maximum and minimum velocity magnitudes along a tagged line was assumed to be equal to the maximum potential spanwise velocity component. This assumption is based upon the knowledge that the dominant velocity components are positive and in the axial direction for both experiments. By multiplying the calculated spanwise velocity component for a particular line by Δt_{ND}, the pixel shift corresponding to the spanwise component for that line was obtained. This procedure was repeated for all lines.

By shifting the delayed image up or down (in the spanwise direction) in 1-pixel increments, and correlating it with the original undelayed image, the axial velocity values in the presence of a uniform spanwise velocity component corresponding to these pixel shifts, is calculated. This is repeated up to the maximum shift value, rounded up to the nearest integral value, encountered for the image set. The root-sum of the squared difference between the unshifted (spanwise) axial velocity values and the pixel-shifted axial velocity values, in both the up and down spanwise directions, is calculated and represents the velocity uncertainty in the axial direction due to a spanwise velocity component corresponding to a particular pixel-shift magnitude. For each tagged line, using the maximum potential spanwise pixel shift magnitude calculated, the axial velocity uncertainty due to this potential spanwise velocity component is interpolated from the axial velocity uncertainty values obtained for the range of pixel-shifted images.

V. Results

A. RCS Jet

Figure 7 shows a flow visualization image and the corresponding field of view imaged by the camera. Figures 8a and 8b show an 87-shot average undelayed image and delayed image, respectively. Figure 8c shows the resulting 87-shot average velocity components and associated uncertainties superimposed over a single-shot flow visualization image. In Fig. 8c, the green ordinate axes are located along the averaged center of maximum signal intensity of the tagged lines in the undelayed image (Fig. 8a) while the green horizontal axes serve as the velocity scale. The enlarged horizontal axis on the far right of Fig. 8c provides the magnitude of the velocity scale. The images were created using the Virtual Diagnostics Interface (ViDI) software developed at NASA Langley Research

Center.[37] The software is based upon Autodesk 3DS Max® software and provides a virtual environment in which experimental data can be combined with virtual models to aid in understanding the related fluid mechanics.

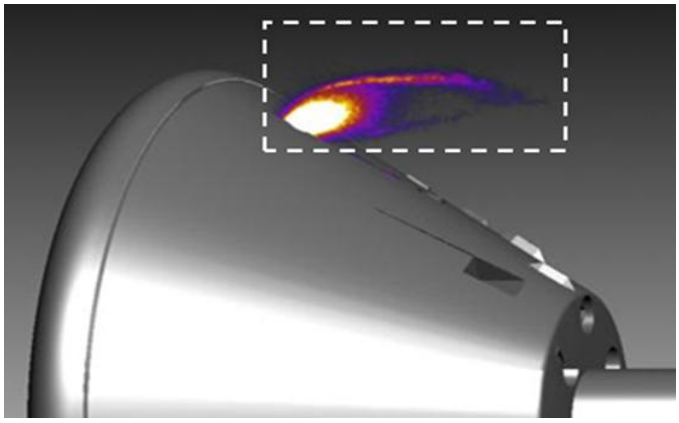

Fig. 7 Orion CEV yaw RCS jet and field of view. A false color table has been applied to the PLIF image, which is displayed using ViDI.

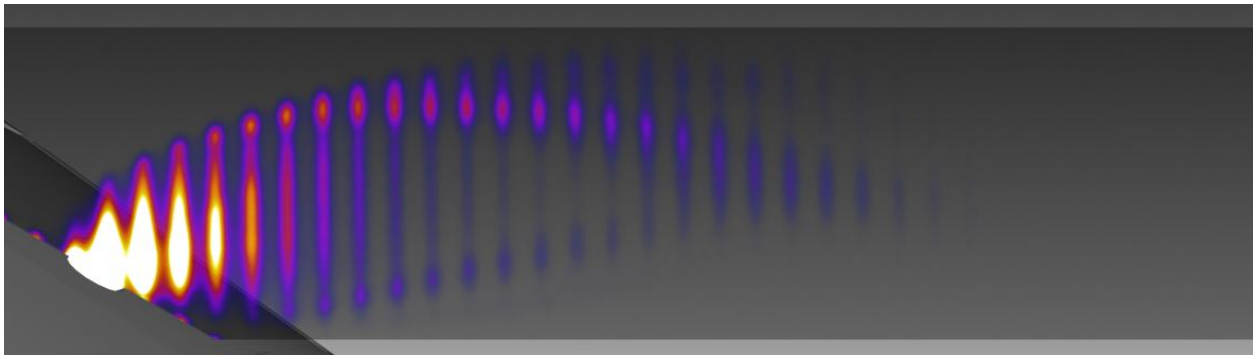

(a)

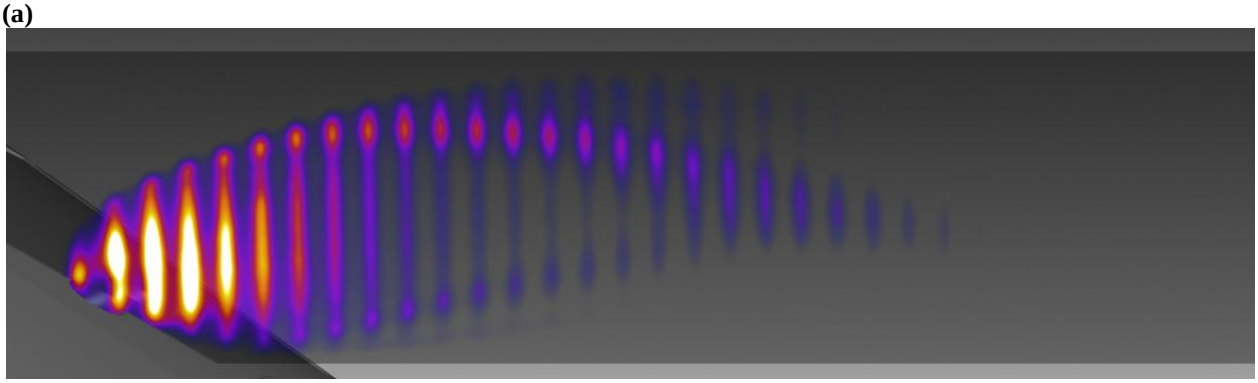

(b)

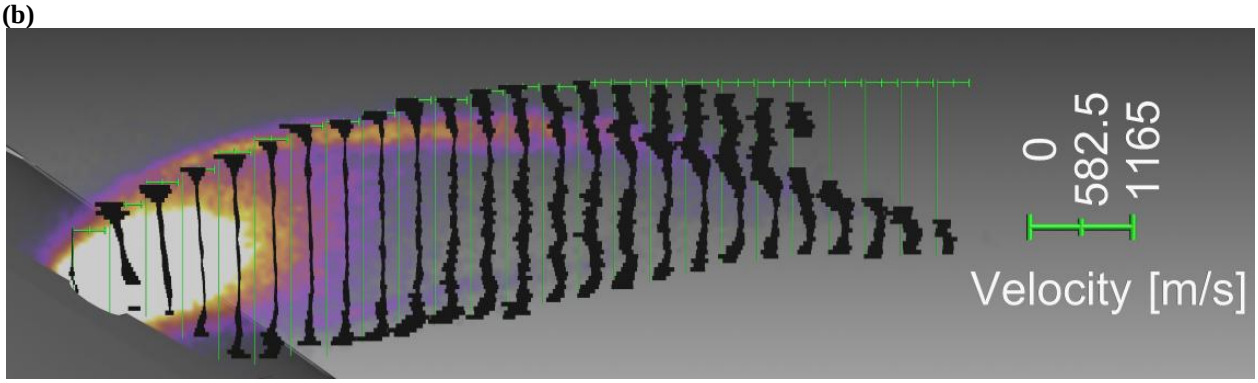

(c)

Fig. 8 Orion CEV yaw RCS jet (a) reference image, (b) shifted image, and (c) velocity (location of center of black bar from green axis) and uncertainty results (bar widths) superimposed on a flow visualization image. False color tables have been applied to the PLIF and MTV images.

In Fig. 8c, the velocity values are represented by the offset of the black horizontal bars from left-hand vertical axes. The width of these bars about the center corresponds to two-times the total uncertainty (Equation 7). Within the core of the RCS jet (lines 5 through 14 downstream of the nozzle), the mean velocity is approximately 669 m/s, with a 42 m/s standard deviation of this mean value. In the regions of highest signal level, such as the along the 1st and 4th profiles within the core region, the mean uncertainties are approximately ±30 m/s and ±44 m/s, respectively. In regions where the signal level is relatively low, such as the downstream region of the core, the total uncertainty noticeably increases. This increased uncertainty is due to the difficulty in correlating lower signal-to-noise regions, which results in difficulties obtaining a highly-peaked polynomial fit of the correlation coefficients. Along the 19th line from the nozzle exit, outside of the core region, the average uncertainty is approximately ±348 m/s.

Near the downstream and boundary regions of the RCS jet, the jet becomes unsteady and begins to fluctuate in the vertical direction of the image plane. This unsteadiness results in intermittent signal in these regions. The signal-to-noise ratio in these regions is also decreased noticeably in comparison to the levels observed at the nozzle exit. These factors result in increased uncertainty. Additionally, large variations in measured average velocities along a single line results in increased spanwise velocity uncertainties.

The most notable deviation from expected velocity occurred along the 2nd profile from the jet exit. The measured velocity of this profile nearest the axis of the nozzle appears to reach a maximum of approximately 895±218 m/s. However, the theoretical maximum velocity the jet can attain at any point is 790 m/s. This value is calculated by assuming the stagnation enthalpy of the room temperature N_2 gas supplied to the RCS jet is completely converted to kinetic energy. Therefore, any points where the combined velocity and uncertainty exceeded the theoretical

maximum velocity value have been discarded. This over-prediction of velocity is due to the role of large quenching gradients in the immediate vicinity of the nozzle exit such that the fluorescence lifetime, τ_{LIF}, on the left side of a tagged line is significantly shorter than on the right side.

For the under-expanded jet, the gas pressure at the exit plane of the nozzle is sufficiently high for quenching to affect the tagged profile. Observing Fig. 8b, the region nearest the jet exit along the 2nd profile is visibly weighted to the right. Due to this right-weighting, the cross-correlation erroneously calculated higher velocities (with associated uncertainties) that exceeded the theoretical maximum velocity obtainable. As the gas exiting the nozzle continues to expand, the gradient in pressure, and hence quenching, becomes insignificant and this velocity discrepancy no longer occurs. Observation of the delayed images suggests that beyond approximately 2 nozzle exit diameters downstream, this effect is negligible. In Fig. 8c, data points vastly exceeding this theoretical limit have been removed.

Figure 9 shows a single-shot velocity and uncertainty measurement of the yaw RCS jet. The increased noise level, compared to the noise level for the averaged velocity measurements, occurring in the single-shot images results in greater velocity uncertainties. Similar to the averaged velocity measurement, regions in the single-shot image pair with relatively higher signal-to-noise levels have lower velocity uncertainties than the lower signal-to-noise regions. For the higher signal-to-noise regions, such as along the 4th profile from the nozzle exit in the jet core, the mean uncertainty is ±133 m/s. For lower signal-to-noise regions, such as in the core region along the 10th profile from the nozzle, the mean uncertainty is ±454 m/s.

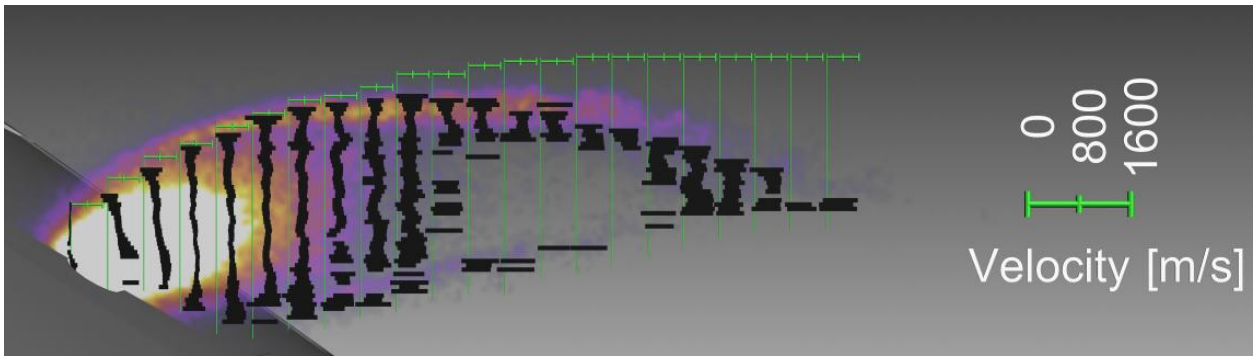

Fig. 9 Single-shot yaw RCS jet velocity and uncertainty measurement.

B. Wedge Model

Figure 10 shows the wedge model with the 2-mm by 4-mm tall cylindrical trip and the corresponding field of view imaged by the camera. Figure 11a shows an averaged PLIF flow visualization image. Figure 11b and 11c show

38-shot averaged the tagged profiles for the undelayed and delayed images, respectively. Figure 11d shows the measured average velocity profiles obtained with the cross-correlation algorithm.

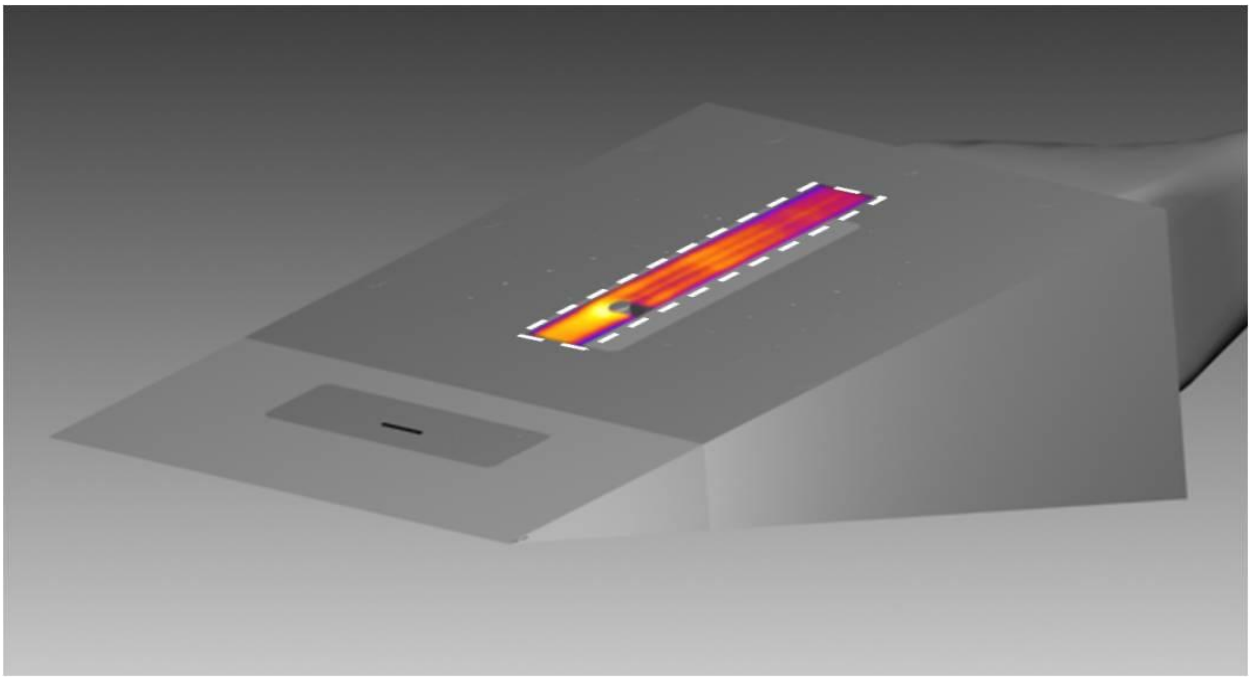

Fig. 10 Perspective view of wedge model, trip, and corresponding field of view.

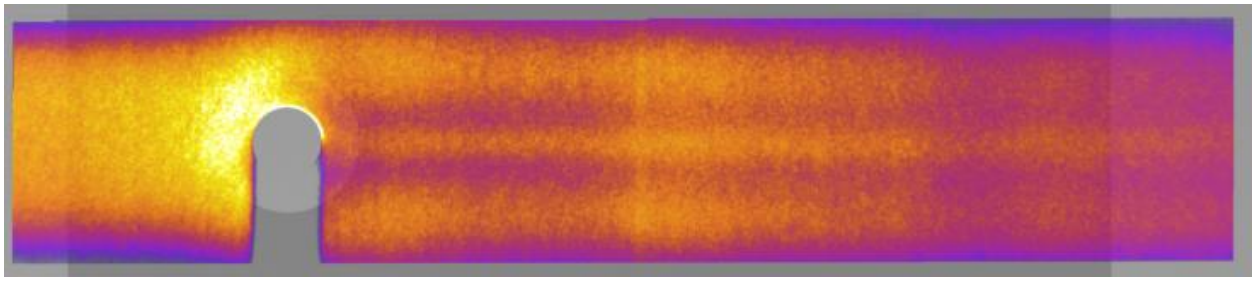

(a)

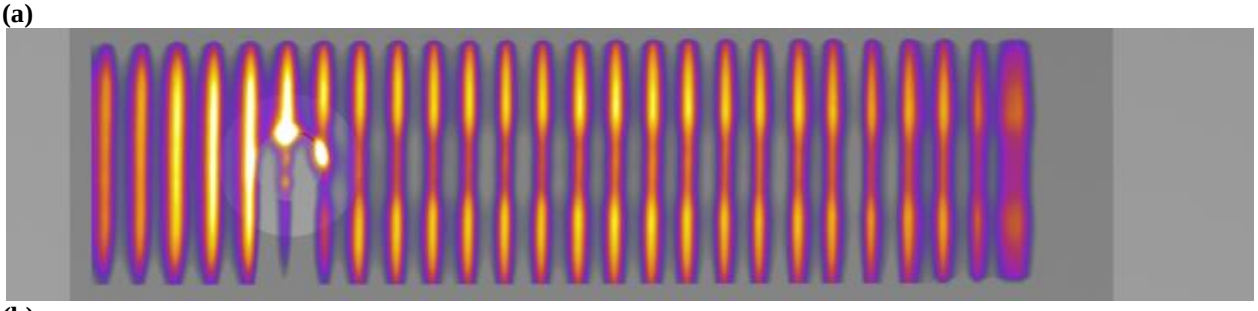

(b)

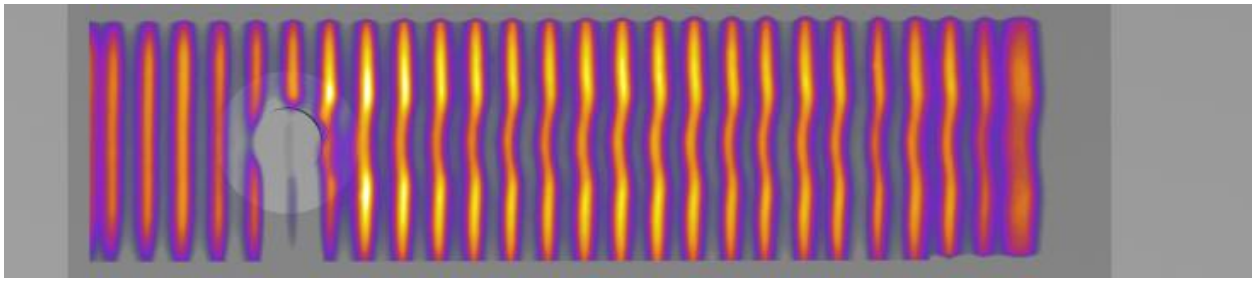

(c)

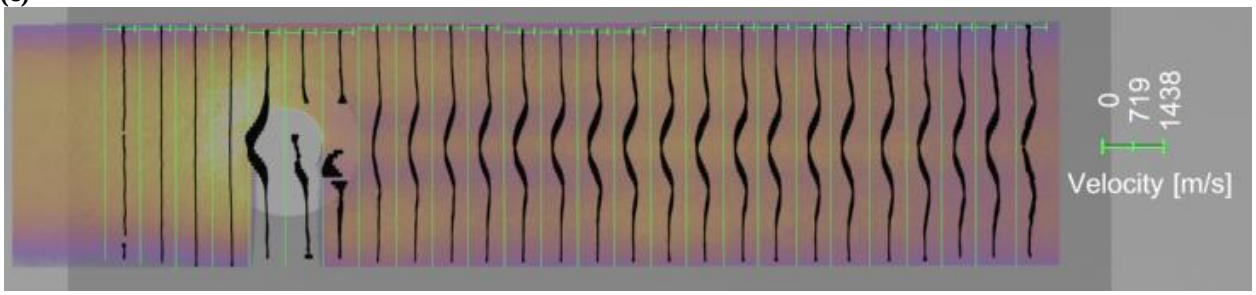

(d)

Fig. 11 Wedge model (a) flow visualization image, (b) reference image, (c) shifted image, and (d) velocity and uncertainty results. Velocity scale (magnified) on the right in (d) is from 0 to 1438 m/s. The center of the black bars with respect to the green vertical lines in (d) are the 38-shot mean velocity values. The width of these bars represents the 95% uncertainty in the mean velocity measurement. Measurement is 2.1-mm above surface of the flat plate.

Figure 11a shows the flow visualization image at approximately 1.7±0.3-mm off the model surface. Prior to passing around the cylindrical boundary layer trip, the boundary layer flow is completely laminar. After the flow passes the trip, the region directly behind the trip shows that some level of disturbance is occurring based upon the variation of signal intensities in this image.

Figure 11d shows the result of the velocity measurement. The measurement was taken approximately 2.1±0.2-mm above the model surface. The velocity scale for this image is 0 to 1438 m/s. In the first two lines upstream of the trip, the flow indeed appears to be nearly uniform and laminar. For the 1st line, the mean velocity along the line is 915 m/s with an average uncertainty of 41 m/s. For the 2nd line, the mean velocity along the line is 1008 m/s with an average uncertainty of 32 m/s. Close examination of the third and forth lines in the region directly upstream of the trip shows a small level of bowing, away from the trip, in the velocity data that could signify some level of interaction with the trip. Along the 3rd line the velocity drops to 905 m/s, along the 4th line it drops to 830 m/s at the point of intersection with the centerline, and the flow is nearly brought to rest in front of the trip. As the flow progresses around the trip, the measured velocities appear to maintain the pre-trip velocity with the exception of the velocity values in the immediate wake of the trip. As the flow passes around the trip, a deficit of velocity extends downstream along the centerline, which is visible even in the raw delayed image shown in Figure 11c. In contrast,

the flow downstream of the upper and lower edge of the trip in these images is accelerated beyond the unperturbed flow velocity occurring upstream of the trip and on the periphery of the image downstream of the trip. Downstream of the trip the velocity observed along the centerline drops to a low of 344 m/s on the 26th line. In the accelerated flow region directly downstream of the top and bottom edges of the trip, the maximum velocity encountered is 1093 m/s on the 22nd line.

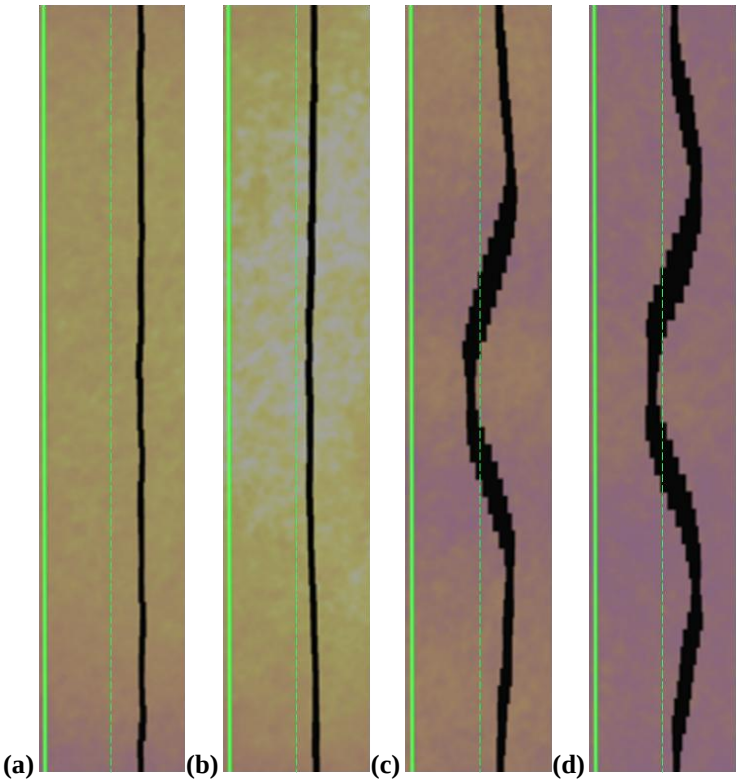

Fig. 12 Magnified view of the mid-portion of the (a) 2nd, (b) 4th, (c) 10th, and (d) 24th mean velocity profiles and their corresponding uncertainties. The dashed green line represents the mid-scale velocity of 719 m/s.

Figure 12 shows from left to right the magnified views of the 2nd, 4th, 10th, and 24th velocity profiles, respectively. The 2nd profile (Fig. 12a) with a mean velocity of approximately 1008 m/s has uncertainties ranging from 27 m/s to 43 m/s. The decreased velocity feature, a left-bowing profile, in the 4th velocity profile (Fig. 12b) gives uncertainty magnitudes ranging from 30 m/s to 43 m/s. The 10th profile (Fig. 12c) shows a drop in velocity along the centerline to approximately 612 m/s. The increased velocities occurring above and below the low-velocity region are approximately 1040 m/s and 1021 m/s, respectively. In regions of steep velocity gradients, the maximum uncertainties encountered along this profile are on the order of 116 m/s to 125 m/s. The largest uncertainty immediately above (with respect to the magnified view) the lowest velocity value is 125 m/s, and is due to the inclusion of the spanwise velocity component uncertainty. The 24th profile in Fig. 12d shows a similar trend to that

of the 10th mean velocity profile. The flow above and below the low velocity region, which has a minimum velocity of 593 m/s, has maximum velocities of 1058 m/s and 1050 m/s, respectively.

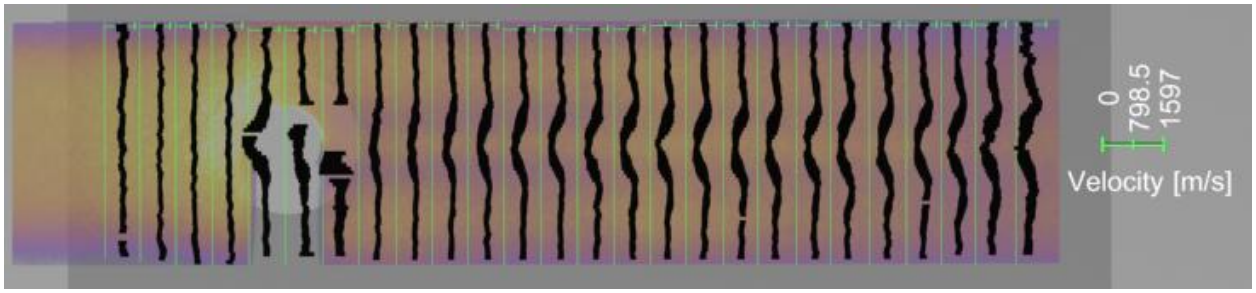

Fig. 13 Single-shot velocity profiles and uncertainty bounds.

Figure 13 shows a single-shot velocity measurement. The decreased signal-to-noise level in the single-shot image (versus the averaged image) results in more variability in the velocity measurements as well as increased uncertainty along each profile. The uncertainties encountered along the 2nd, 4th, 10th, and 24th profiles in this single-shot velocity measurement varied from 98 m/s to 192 m/s, 118 m/s to 183 m/s, 117 m/s to 277 m/s, and 131 m/s to 615 m/s, respectively.

VI. Discussion

The double-shutter camera used in both the Orion CEV and wedge experiments served to reduce measurement sensitivity to vibration that would otherwise be encountered in a single-framing camera velocity measurement [7] where delayed images are compared with an undelayed image separately acquired and uncorrelated in time. The double-shutter camera velocity measurement was also free of errors encountered when using a two-camera velocimetry system, which is also sensitive to vibration. However, the hardware-limited 500 ns gate delay between the undelayed and delayed images and the limitation of a single gain setting for both images resulted in reduced signal levels in the delayed image. To compensate for this decreased signal level, a timing methodology was developed in which the 1st gate was partially overlapped with the laser pulse so that only a fraction of the fluorescence from the tagged velocity profiles would be acquired in the first exposure, resulting in comparable signal levels in the undelayed and delayed image. Additionally, by varying the length of the 2nd gate, the amount of fluorescence acquired in the second exposure could be controlled to some level. However, by increasing the 2nd gate, the level of blurring and asymmetry of the tagged profile in the 2nd exposure also increased. To account for this, a correction was applied that was dependent upon the signal intensity ratios between the undelayed and delayed profiles (and implicitly on the fluorescence lifetime), the overlap between the laser pulse and effective 1st gate, as

well as the duration of the second gate. This correction was independent of the flow velocity and the methodology can be extended to 2-dimensional MTV measurements.

Table 5. Constituent uncertainty term analysis for wedge experiment for an average of N = 38 images.

	2nd Profile: $\bar{V}_{AVG}$ = 1008 m/s Mean % of $\bar{V}_{AVG}$	$(dV_{AVG}/dy)\|_{max}$ Mean % of V_{AVG}
$u_{V,\text{Magnification}}$	0.15	0.15
$u_{V,\text{Accuracy}}$	0.99	1.27
$u_{V,\text{Spanwise}}$	0.13	15.45
$\sqrt{u_{V,\Delta x}^2 + u_{V,\Delta t}^2}\begin{cases}u_{V,\Delta x}\\u_{V,\Delta t}\end{cases}$	$1.93\begin{cases}1.88\\0.41\end{cases}$	$4.10\begin{cases}4.08\\0.41\end{cases}$
u_V	3.20	20.97

In relatively good signal-to-noise regions with uniform axial velocity components along the length of the tagged profile, the measured velocity uncertainty is on the order of 3 percent (30 m/s for a 1000 m/s flow). In regions where the signal-to-noise ratio remains relatively high but large axial velocity gradients exist, the measured velocity uncertainty is on the order of 20 percent. Table 5 provides a listing of the mean constituent uncertainty magnitudes for the wedge experiment based upon Equation 7. The left data column of Table 5 provides these values for the 2nd profile. The right data column contains the mean constituent uncertainty magnitudes at two points on opposite sides of the centerline for profiles 11 through 25 where the maximum spanwise velocity uncertainty is encountered. These points correspond to the location where the axial velocity gradients are at a maximum. The total uncertainties, as a percentage of the average velocity, represent the extremes of the uncertainty magnitudes encountered in the wedge experiment. To obtain a coarse estimate of the magnitude of the single-shot uncertainties, the precision uncertainty terms can be multiplied by $\sqrt{N}$, where N is the number of image pairs use to make the averaged velocity measurement.

Based upon the measurements observed in this experiment and the simulations performed to determine the correction factor, we determined that using a shorter second gate (100 ns in the wedge experiment) would limit the greater variability encountered in the correction factor when a longer gate (300 ns in the CEV experiment) is employed. This is detailed in Fig. 5. An alternative way to avoid the variability due to the correction factor and its associated uncertainty is by generating the profile molecules (NO) prior to the start of the first gate via photodissociation of NO_2 [14]. The tagged gas lines generated could then be optically excited with a laser source prior to, and captured by, the first and second gates, both of equal durations. This method would result in similarly shaped spatial fluorescence profiles, would generally not require any correction for profile asymmetry, and would

remove any uncertainties associated with the overlap of the 1st gate and the firing of the excitation laser. Another benefit of such a scheme would be the removal of timing dependence on fluorescence lifetime. This would allow for increased temporal separation between the undelayed and delayed images, resulting in decreased uncertainties proportional to the increased separation time, and the ability to work in higher-pressure conditions where fluorescence quenching would otherwise prohibitively limit the signal in the second gate. Difficulties with this technique include seeding NO_2 safely into the flow, the use of higher laser energies in order to dissociate the NO_2, the heavier molecular weight of the NO_2 molecule with respect to air, and the presence of collisional quenching gradients.

One issue encountered when making RCS jet velocity measurements was the over-estimation of jet velocity in the immediate vicinity of the nozzle exit (Fig. 8c and Fig. 9). As the gas exits the nozzle in this region, a rapid drop in pressure occurs, resulting in a negative collisional quenching gradient. The result of this gradient, as observed in Fig. 8b, is a perceived shift in the tagged profile much greater than expected. Therefore, in the presence of a negative collisional quenching gradient, the measured velocities will be higher than those measured if no gradient were present. Figure 14 shows the results of a simulation performed to analyze the effects of such a gradient. For this simulation, t_{eG1}= 8.25 ns, t_P= 9.5 ns, and t_{G2}= 100 ns.

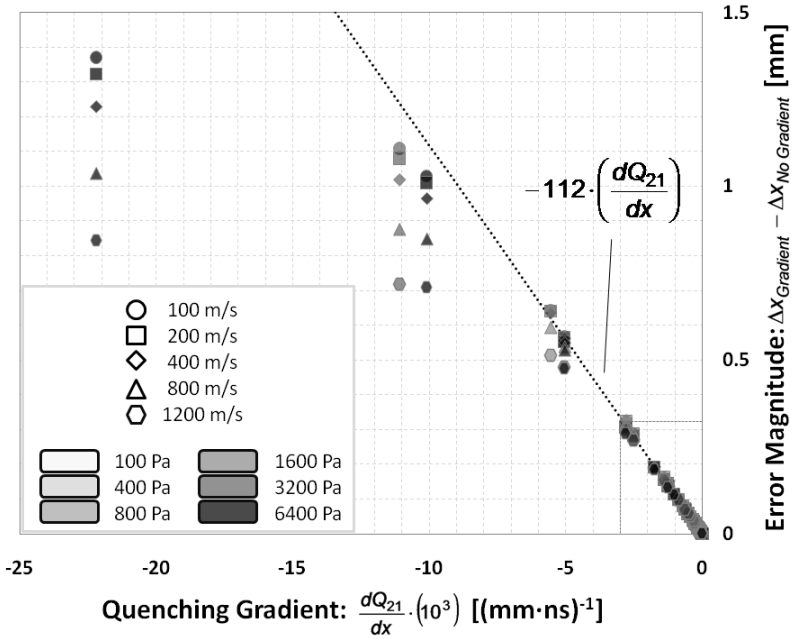

Fig. 14 Non-zero quenching gradient influence on perceived profile shift.

In the simulation, a 19-pixel FWHM excitation source located 2 pixels to the left of a 55-pixel wide correlation window was used. At the center of the correlation window, the pressure (and hence quenching rate), was set to a

particular value, noted in the legend of Fig. 14. Additionally, for each pressure condition, an axial velocity magnitude ranging from 100 m/s to 1200 m/s was simulated to see what, if any, effect gas velocity had on skewing of the velocity measurement in the presence of a quenching gradient. In Fig. 14, the horizontal axis corresponds to the magnitude of the quenching gradient simulated. The vertical axis in this figure corresponds to the difference between the profile shift measured, in pixels, for the case with ($\Delta x_{Gradient}$) and without ($\Delta x_{No\ Gradient}$) a quenching gradient present. For relatively weak gradient values (> -3 [ns·mm]$^{-1}$), $\Delta x_{Gradient}$ scales linearly with $\Delta x_{No\ Gradient}$ as the magnitude of the gradient increases, as shown in Fig. 14. Over this range of gradient magnitudes, the effect of the gradient is approximately independent of velocity, and can be defined by the relation:

$$\Delta x_{Gradient} \approx -112 \cdot \left(\frac{dQ_{21}}{dx}\right) + \Delta x_{No\ Gradient},\ -3 < \frac{dQ_{21}}{dx} < 0 \tag{14}$$

This influence manifests itself most strongly during the 2nd gate, when the quenching field determines the spatial shape of the fluorescence profile. Beyond this point, the velocity of the tagged profile begins to affect $\Delta x_{Gradient}$. As the magnitude of the quenching gradient increases, increases in the gas velocity have the effect of decreasing the influence of the gradient on $\Delta x_{Gradient}$. This is because the increased velocity places the profile into a region where the quenching is much less than that at the center of the correlation window where the profile was initially tagged, resulting in a right-weighting of the perceived profile. As the quenching gradient magnitude exceeds 6 [ns·mm]$^{-1}$, increases in collisional quenching at the center of the correlation window will begin to further left-weight the profile observed in the 2nd exposure. This in turn counteracts the right-weight occurring due to the presence of the gradient.

A significant contribution to the total velocity uncertainty in both the mean and single-shot velocity measurements was the accuracy measurement. After the CEV and wedge experiments were performed, it was learned that there was the potential for small velocities within the test section when it was reduced to near vacuum due to leaks in the system. If a non-zero gas velocity field did indeed exist within the test section during acquisition of the zero-velocity images, the resulting accuracy value would be skewed from a true zero value, leading to an underestimation of the true accuracy of the measurement. Measurements along individual lines from these images seem to confirm this hypothesis, as non-zero velocities were observed with trends that appear to have a functional relationship with the tunnel pressure. Correction of this may result in lower velocity uncertainties in both mean and single-shot velocity measurements due to improved accuracy estimation. A possible solution is to have a static cell

at the tunnel pressure which can be imaged separately to obtain a measure of velocity accuracy. Such a measure could potentially improve experimental accuracy.

VII. Conclusion

This paper describes a velocimetry technique using a single, double-frame camera to obtain spatially and temporally correlated images. A new method was developed to acquire the undelayed and delayed images so that comparable signal intensities would be obtained in both exposures. A correction technique was also introduced which estimated the perceived profile shift observed in the delayed image due to fluorescence decay. Single-shot and mean velocities and uncertainties were calculated for an Orion CEV yaw RCS jet and a 10-degree half-angle wedge in a Mach 10 perfect gas air flow. Errors associated with spanwise velocity components (parallel to the laser sheet) were quantified for the first time. A discussion of the contribution of collisional quenching gradients to the skewing of the velocity measurement was also provided.

Acknowledgments

We wish to acknowledge the expert contribution to this work from the 31-Inch Mach 10 Air Tunnel and data system operators at NASA Langley Research Center. This work was supported by NASA's Fundamental Aeronautics Program, Hypersonics Project, Experimental Capabilities and Aerodynamics, Aerothermodynamics, and Plasma Disciplines.

References

[1] Everhart, J.L., "*Transition Induced by Fence Geometries on Shuttle Orbiter at Mach 10*," AIAA-2010-1577, 48th AIAA Aerospace Sciences Meeting, Orlando, FL, January 4-7, 2010.

[2] Berry, S.A., Auslander, A.H., Dilley, A.D., and Calleja, J.F., "*Hypersonic Boundary-Layer Trip Development for Hyper-X*," Journal of Spacecraft and Rockets, 38 (6), November-December, 2001.
doi: 10.2514/2.3775

[3] Danehy, P.M., Wilkes, J.A., Brauckmann, G.J., Alderfer, D.W., Jones, S.B., and Patry, D.P., "*Visualization of a Capsule Entry Vehicle Reaction-Control System (RCS) Thruster*," AIAA 2006-1532, 44th AIAA Aerospace Sciences Meeting and Exhibit, January 9-12, 2006, Reno, NV.

[4] Johnson, S., and Murphy, K., "*Pressure-Sensing Performance of Upright Cylinders in a Mach 10 Boundary-Layer*," NASA Technical Memorandum 4633, July, 1994.

[5] Koochesfahani, M.M., "*Molecular Tagging Velocimetry (MTV): Progress and Applications*," AIAA 1999-3786, 30th AIAA Fluid Dynamics Conference, June 28 – July 1, 1999.

[6] Hiller, B., Booman, R.A., Hassa, C., and Hanson, R.K., "*Velocity visualization in gas flows using laser-induced phosphorescence of biacetyl*," Rev. Sci. Instrum., 55 (12), December, 1984.
doi: 10.1063/1.1137687

[7] Danehy, P.M., O'Byrne, S., Houwing, A.F.P, Fox, J.S., and Smith, D.R., "*Flow-Tagging Velocimetry for Hypersonic Flows Using Fluorescence of Nitric Oxide*," AIAA Journal, 41 (2), February, 2003.
doi: 10.2514/2.1939

[8] Lempert, W.R., Boehm, M., Jiang, N., Gimelshein, S., and Levin, D., "*Comparison of molecular tagging velocimetry data and direct simulation Monte Carlo simulations in supersonic micro jet flows*," Experiments in Fluids, 34, pp. 403-411, 2003.
doi: 10.1007/S00348-002-0576-7

[9] Inman, J.A., Danehy, P.M., Bathel, B.F., and Nowak, R.J., "*Laser Induced Fluorescence Velocity Measurements in Supersonic Underexpanded Impinging Jets*," 48th AIAA Aerospace Sciences Meeting, AIAA Paper 2010-1438, January 4-7, 2010, Orlando, FL.

[10] Stier, B., Koochesfahani, M.M., "*Molecular Tagging Velocimetry (MTV) measurements in gas phase flows*," Experiments in Fluids, 26, pp. 297-304, 1999.
doi:10.1007/S00348-005-0292

[11] Orlemann, C., Schulz, C., and Wolfrum, J., "*NO-flow tagging by photodissociation of NO_2. A new approach for measuring small-scale flow structures*," Chem. Phys. Lett., 307, pp. 15-20, 1999.
doi: 10.1016/S0009-2614(99)00512-6

[12] Shinji, N., Kasahara, M., Tsue, M., and Kono, M., "*Velocity Measurements of Reactive and Non-reactive Flows by NO-LIF Method Using NO_2 Photodissociation*," Heat Transfer – Asian Research, 34 (1), pp. 40-52, 2005.
doi: 10.1002/htj.20038

[13] Hsu, A.G., Srinivasan, R., Bowersox, R.D.W, and North, S.W., "*Molecular Tagging Using Vibrationally Excited Nitric Oxide in an Underexpanded Jet Flowfield*," AIAA Journal, 47 (11), November, 2009.
doi: 10.2514/1.47716

[14] Hsu, A.G., Srinivasan, R., Bowersox, R.D.W., and North, S.W., "*Two-component molecular tagging velocimetry utilizing NO fluorescence lifetime and NO_2 photodissociation techniques in an underexpanded jet flowfield*," Applied Optics, 48 (22), pp. 4414-4423, August, 2009.
doi: 10.1364/AO.48.004414

[15] Dam, N.J., Klein-Douwel, R.J.H., Sijtsema, N.M., and ter Meulen, J.J., "*Nitric oxide flow tagging in unseeded air*," Optics Letters, 26 (1), pp. 36-38, January 1, 2001.
doi: 10.1364/OL.26.000036

[16] Sijtsema, N.M., Dam, N.J., Klein-Douwel, R.J.H., and ter Meulen, J.J., "*Air Photolysis and Recombination Tracking: A New Molecular Tagging Velocimetry Scheme*," AIAA Journal, **40** (6), June 2002.
doi: 10.2514/2.1788

[17] Van der Lann, W.P.N, Tolboom, R.A.L., Dam, N.J., and ter Meulen, J.J., "*Molecular tagging velocimetry in the wake of an object in supersonic flow*," Experiments in Fluids, 34, pp. 531-534, 2003.
doi: 10.1007/S00348-003-0593-1

[18] Boedeker, L.R., "*Velocity measurement by H2O photolysis and laser-induced fluorescence of OH*," Optics Letters, 14 (10), pp. 473-475, May 15, 1989.
doi: 10.1364/OL.14.000473

[19] Wehrmeyer, J.A., Ribarov, L.A., Oguss, D.A., Batliwala, F., Pitz, R.W., and DeBarber, P.A., "*Flow tagging velocimetry for low and high temperature flowfields*," *37th AIAA Aerospace Sciences Meeting*, Reno, NV, 1999.

[20] Wehrmeyer, J.A., Ribarov, L.A., Oguss, D.A., and Pitz, R.W., "*Flame flow tagging velocimetry with 193-nm H2O photodissociation*," Applied Optics, 38 (33), pp. 6912-6917, November, 20, 1999.
doi: 10.1364/AO.38.006912

[21] Pitz, R.W., Brown, T.M., Nandula, S.P., Skaggs, P.A., DeBarber, P.A, Brown, M.S., and Segall, J., "*Unseeded velocity measurement by ozone tagging velocimetry*," Optics Letters, 21 (10), pp. 755-757, 1996.
doi: 10.1364/OL.21.000755

[22] Miles, R., Cohen, C., Connors, J., Howard, P., Huang, S., Markovitz, E., and Russell, G., "*Velocity measurements by vibrational tagging and fluorescent probing of oxygen*," Optics Letters, 12 (11), pp. 861-863, November, 1987.
doi: 10.1364/OL.12.000861

[23] Gendrich, C.P, and Koochesfahani, M.M., "*A spatial correlation technique for estimating velocity fields using molecular tagging velocimetry (MTV)*," Experiments in Fluids, Vol. 22, pp. 67-77, 1996.
doi: 10.1007/BF01893307

[24] Thomson, S.L. and Maynes, D., "*Spatially Resolved Temperature Measurements in a Liquid Using Laser Induced Phosphorescence*," Journal of Fluids Engineering, 123 (2), pp. 293-302, June 2001.
doi: 10.1115/1.1365960

[25] Hu, H. and Koochesfahani, M.M., "*Molecular tagging velocimetry and thermometry and its application to the wake of a heated circular cylinder*," Meas. Sci. and Technol., 17 (6), pp. 1269-1281, 2006.
doi: 10.1088/0957-0233/17/6/S06

[26] Hu, H., Koochesfahani, M.M., and Lum, C., "*Molecular tagging thermometry with adjustable temperature sensitivity*," Experiments in Fluids, 40, pp. 753-763, 2006.
doi: 10.1007/S00348-006-0112-2

[27] Buck, G.M., Watkins, A.N., Danehy, P.M., Inman, J.A., Alderfer, D.W., and Dyakonov, A.A., "*Experimental Measurement of RCS Jet Interaction Effects on a Capsule Entry Vehicle*," 46th AIAA Aerospace Sciences Meeting and Exhibit, AIAA-2008-1229, Orlando, FL, January 7-10, 2008.

[28] Danehy, P.M., Ivey, C.B., Inman, J.A., Bathel, B.F., Jones, S.B., Jiang, N., Webster, M., Lempert, W., Miller, J., and Meyer, T., "*High-speed PLIF imaging of hypersonic transition over discrete cylindrical roughness*," AIAA-2010-0703, 48th AIAA Aerospace Sciences Meeting, Orlando, FL, January 4-7, 2010.

[29] Danehy, P.M., Bathel, B.F., Ivey, C., Inman, J.A., and Jones, S.B., "*NO PLIF study of hypersonic transition over a discrete hemispherical roughness element*," AIAA 2009-394, 47th AIAA Aerospace Sciences Meeting, January 5-8, 2009, Orlando, Florida.

[30] Micol, J.R., "*Langley Aerothermodynamic Facilities Complex: Enchancements and Testing Capabilities*," AIAA 1998-0147, 36th AIAA Aerospace Sciences Meeting, January 12-15, 1998, Reno, Nevada.

[31] Berry, S.A., Nowak, R.J., and Horvath, T.J., "*Boundary Layer Control for Hypersonic Airbreathing Vehicles*," AIAA 2004-2246, 34th AIAA Fluid Dynamics Conference and Exhibit, June 28 – July 1, 2004, Portland, Oregon, 2004.

[32] Alderfer, D.W., Danehy, P.M., Wilkes Inman, J.A., Berger, K.T., Buck, G.M., and Schwartz, R.J., "*Fluorescence Visualization of Hypersonic Flow Over Rapid Prototype Wind-Tunnel Models*," AIAA 2007-1063, 45th Aerospace Sciences Meeting and Exhibit, Reno, NV, January 8-11, 2007.

[33] Sanchez Sorzano, C.O., Thevenaz, P., and Unser, M., "*Elastic Registration of Biological Images Using Vector-Spline Regularization*," IEEE Transactions on Biomedical Engineering, 52 (4), pp. 652-663, April, 2005.
doi: 10.1109/TBME.2005.844030

[34] Rasband, W.S., ImageJ, U. S. National Institutes of Health, Bethesda, MD, USA, http://rsb.info.nih.gov/ij, 1997-2009.

[35] Settersten, T.B., Patterson, B.D., and Carter, C.D., "*Collisional quenching of NO A2Σ+(v'=0) between 125 and 294 K*," Journal of Chemical Physics, Vol. 130, 2009.
doi: 10.1063/1.3138178

[36] Settersten, T.B., Patterson, B.D., and Humphries IV, W.H., "*Radiative lifetimes of NO A2Σ+(v'=0,1,2) and the electronic transition moment of the A2Σ+-X2Π system*," Journal of Chemical Physics, Vol. 131, 2009.
doi: 10.1063/1.3227520

[37] Schwartz, R.J., "*ViDI: Virtual Diagnostics Interface Volume 1-The Future of Wind Tunnel Testing*," Contractor Report NASA/CR-2003-212667, December, 2003.